Soft Matter

Accepted Manuscript

This article can be cited before page numbers have been issued, to do this please use: S. R. R. Kalghatgi, S. P. Thampi, S. Kumar and C. Durning, *Soft Matter*, 2026, DOI: 10.1039/D6SM00323K.

ROYAL SOCIETY OF CHEMISTRY

rsc.li/soft-matter-journal

View Article Online
DOI: 10.1039/D6SM00323K

Soft Matter

ARTICLE TYPE

Cite this: DOI: 00.0000/xxxxxxxxxx

Modeling Domain Growth of Polymer Melt Crystallization

Sameer Rajendra Kalghatgi,[a] Sumesh P. Thampi,[‡b], Sanat K. Kumar,[*a] and Christopher J. Durning[†a]

Received Date
Accepted Date

DOI: 00.0000/xxxxxxxxxx

The crystallization of a subcooled polymer melt, described by a local scalar internal variable ϕ, is modeled by non-equilibrium thermodynamics, specifically using a dissipation argument. The formulation yields a pair of nonlinear differential equations: a thermal energy balance coupled to a Fisher-type rate law for melt to solid conversion. The simplest non-dimensional forms of these equations have two parameters: the Stefan number λ, quantifying the relative importance of latent heat release to conductive heat transport, and a dispersion coefficient β for secondary melt nucleation. Traveling wave solutions for the temperature and ϕ result in both 1 and 2 dimensions for realistic λ and β [$\lambda \gtrsim \mathcal{O}\left(10^0\right)$; $\beta \lesssim \mathcal{O}\left(10^{-1}\right)$]. The prediction of sharp solidification fronts controlled by crystallization kinetics is consistent with experiments on polymer melts. Specifically, the undercooling at the solid/melt interface scales with the front speed. The equilibrium extent of solidification is controlled by λ and thermal constraints, while β determines the front speed. The model predictions are robust in that neither the details of temperature dependencies in the source/nucleation terms, nor the inclusion of solid/melt interfacial energy, qualitatively affects predictions. Together with a specification of primary nucleation kinetics, the model can successfully simulate overall crystallization kinetics.

1 Introduction

Semicrystalline polymers are of primary importance in applications that demand favorable mechanical properties, and thermal/chemical stability[1]. Industrial-scale production for such applications typically involves crystallization from the melt, resulting in unique, hierarchical semi-crystalline morphologies. In the absence of external fields, sub-cooled flexible polymer melts crystallize into "spherulites" with size $\sim 1-100$ μm. The polymer spherulite consists of radially organized, lamellar crystals mixed with disordered, amorphous material. The lamellae are flat, ribbon-like structures of broad surface with a thin dimension of $\sim \mathcal{O}(1-10)$ nm. Remarkably, the chain axis runs nearly along the thin lamellar dimension, implying a chain folding process involved in the crystallization. The intra-spherulite lamellae appear to stack, with alternating crystal and amorphous layers having a periodicity $\sim \mathcal{O}(1-10)$ nm (i.e., the "long-spacing"). Thus, spherulites are themselves semicrystalline, incorporating a significant amorphous-crystal interface. The systematic control and manipulation of this hierarchical structure can be achieved using external fields (thermal, electrical, magnetic) to produce high-performance/high-value semi-crystalline polymeric and functional polymer-inorganic hybrid materials. Previously, we have demonstrated this concept using directional solidification, where an external thermal gradient is imposed during the crystallization of a blend of polyethylene oxide (PEO) and amorphous poly(methyl methacylate) (PMMA)[2]. Unique semicrystalline morphologies were achieved featuring stacked, uniaxially oriented, PEO lamellae with interlayers of amorphous PMMA mixed with PEO. To understand and optimize the use of external fields an accurate mesoscale model for polymer crystallization is required, which is the goal of the present work.

A common scenario is the crystallization of a quenched polymer melt that is uniformly subcooled. Here, primary nucleation initiates the formation of spherulites, and their subsequent growth is by an interfacial process. This process continues until the growing spherulites impinge upon one another. In the first phase, for a polymer melt close to its melting point T_m, spherulites grow at a nearly constant rate G ($[=] L/T$), $G \sim \exp\left(-\frac{B}{\Delta T_0}\right)$ where B is a constant, and $\Delta T_0 = T_m - T_0 > 0$ is the imposed under cooling. Before impingement, spherulites grow isotropically as space-filling geometric objects (i.e., as spheres or disks).

[a] Department of Chemical Engineering, Columbia University, New York, New York 10027, United States.
[b] Department of Chemical Engineering, Indian Institute of Technology Madras, Chennai 600036, India.
[‡] Tel: +91 44 2257 4179; E-mail: sumesh@iitm.ac.in
[*] Tel: +1 3473515314; E-mail: sk2794@columbia.edu
[†] Tel: +1 6469427986; E-mail: cjd2@columbia.edu

View Article Online
DOI: 10.1039/D6SM00323K

There exists a considerable literature modeling G, the secondary nucleation process, from a microscopic perspective[3]. Nearly all of them assume isothermal conditions for deriving $G(\Delta T_0)$ which means that the self-generated thermal field resulting from latent heat release is ignored. This thermal field is considered to be responsible for the solidification front instabilities and consequent dendritic crystal formation common for low molecular weight species[4,5]. The model of Lauritzen and Hoffman (L-H)[3,6] assumes a sharp melt/crystal interface, with G controlled by the crystallographic addition of short clips of chain backbone, i.e. of "stems", from the melt to the tips of the radially oriented lamellar crystals at the edge of a growing spherulite. This addition is postulated to involve a melt/crystal interfacial energy barrier leading to the rate law mentioned above, and selection of a stem length. However, recent models[7–10] and computer simulations[11,12] challenge the mechanistic details asserted by this treatment. In particular, rather than the controlling step of stem attachment at a sharp crystal/melt interface, a relatively broad partially disordered interfacial zone is found along the growth direction. These results thus assert the important role of chain segment attachment to the fully crystalline edge surfaces, with larger length scale chain rearrangements and associations occurring in a partially ordered zone adjacent to the growing crystal surface leading to lamellar extension along the growth direction. These efforts implicate chain conformational entropy, contributing to a free energetic barrier, controlling G. Thus, the secondary nucleation may more resemble a dispersion mediated barrier crossing localized at the growth front, rather than the simple interfacial barrier crossing envisioned in the L-H model.

Mesoscale (hydrodynamic) level modeling of solidification of low molecular weight melts often define a local extent of crystallization, or "order parameter" field, $\phi(\mathbf{r},t)$, indicating the local state. Thus, $\phi = 1 \Rightarrow$ implies a fully solidified state; $\phi = 0 \Rightarrow$ liquid. Stefan's model[13] which assigns $\phi = 1$ (solid) to regions where $T(\mathbf{r},t) < T_m$ and $\phi = 0$ (liquid) where $T(\mathbf{r},t) > T_m$ asserts diffusive heat transport in both the liquid and solid domains, but subject to an interfacial energy balance boundary condition at the isotherm $T_S(\mathbf{r},t) = T_L(\mathbf{r},t) = T_m$ separating the liquid and solid domains. The model implies instantaneous conversion of liquid to solid at T_m. Analytical solutions in one-dimension for solidification of a subcooled melt initially at $T_0 < T_m$ predict $G \sim 1/\sqrt{t}$ with a relatively weak algebraic dependence on undercooling. Further, in two and three-dimensions, the solidification front motion is unstable due to thermal transport limitations, leading to solid growth front ramification and dendritic solid structures[5]. Clearly, the Stefan model and its variations cannot capture the essential features of polymer melt crystallization. A primary reason is the absence of intrinsic crystallization kinetics in the model. To address this deficiency, we have pursued phenomenological modifications to include intrinsic crystallization kinetics and local latent heat release[14–17] to model directional solidification of a melt just above T_m, driven by a moving heat sink at T_0 below T_m. This model verified the long-standing ansatz of a speed-dependent effective undercooling during directional solidification, first articulated by Lovinger and Gryte[18], as well as a maximum possible speed for directional solidification. However, the approach cannot model the solidification of a uniformly sub-cooled melt due to the simplified treatment of secondary nucleation.

An alternative approach exploits the Ginzburg-Landau formalism[19–21]. The theory prescribes the relaxational dynamics of a system initially out of equilibrium, in which new phases can emerge, in terms of an "order parameter" field $\phi(\mathbf{r},t)$. The model specifies the instantaneous (extensive) system free energy A as a density functional, accounting for interfacial free energy via gradient terms. The relaxation to equilibrium minimizes the free energy of the entire system. This formulation, frequently referred to as "Model A"[21], has been applied to study solidification[20,22,23]. However, this method only remains suitable to model low molecular weight systems where the details of crystallization kinetics is rather less important, unlike polymer systems.

In this work, we develop a mesoscale model for solidification using a non-equilibrium thermodynamic (NET) framework. We analyze an incompressible motionless medium with an intensive scalar internal variable $\hat{\phi}(\mathbf{r},t)$ proportional to the local average conversion to solid. The development enforces that the local rate of entropy production Σ be non-negative, and ensures the equilibrium states be the minimum of Σ. The general development produces a pair of coupled, nonlinear partial differential equations (PDEs) governing the temperature, $T(\mathbf{r},t)$, and $\hat{\phi}(\mathbf{r},t)$. The overall structure of the model is remarkably similar to model A but with important differences, which we will clarify. This paper is organized as follows. In section Non Equilibrium Thermodynamics Model Development, we provide a summary of the thermodynamic development. A simplified form of the model, linearized with respect to temperature along with numerical solutions for adiabatic solidification in one dimension are discussed in section Numerical solutions. Section Application of NET Model to 1-D Solidification shows that the equilibrium states predicted by the model are consistent with the equilibrium phase diagram. Section Model Modifications presents scaling, numerical, and phase space analyzes yielding a simple analytical result for the traveling wave speed. Section Two Dimensional Systems summarizes the model's capacity to describe aspects of solidification specific to polymer melts: front speed-dependent effective under-cooling (Lovinger-Gryte anzatz), inclusion of the Gibbs Thomson effect, dimension independent growth kinetics, and that spherulites grow as space filling objects.

2 Non Equilibrium Thermodynamics Model Development

Consider a rigid media whose local state depends on the local $T(\mathbf{r},t)$ (hereforth termed as T) and $\hat{\phi}(\mathbf{r},t)$ $\left(\hat{\phi}\,[=]\,\frac{1}{M}\right)$. In the stationary lab frame we have balance laws:

$$\rho\frac{\partial}{\partial t}\hat{\phi} + \boldsymbol{\nabla}\cdot\boldsymbol{\phi} - \rho\hat{\sigma}_\phi = 0 \tag{1}$$

$$\rho\frac{\partial}{\partial t}\hat{U} + \boldsymbol{\nabla}\cdot\mathbf{q} = 0 \tag{2}$$

where $\boldsymbol{\phi}$ and $\hat{\sigma}_\phi$ are the local flux and specific rate of production of $\hat{\phi}$, respectively. Similarly, $\hat{U}$ and $\mathbf{q}$ are the local specific internal energy and energy flux. The local internal energy depends on

View Article Online
DOI: 10.1039/D6SM00323K

the T, and $\hat{\phi}$. Any dynamic process obeying these balance laws is subject to the second law of thermodynamics,

$$\Sigma = \rho \frac{\partial}{\partial t}\hat{S} + \boldsymbol{\nabla}\cdot\mathbf{s} \geq 0 \tag{3}$$

where $\hat{S}$ and $\mathbf{s}$ are the specific entropy and entropy flux respectively.

To ensure that T has the usual definition at equilibrium, we include the relation $\hat{A} = \hat{U} - T\hat{S}$ where $\hat{A}$ is the local specific free energy and presume $\hat{A}$ depends on T as it does at equilibrium. Consequently $\left(\frac{\partial \hat{A}}{\partial T}\right) = -\hat{S}$. A sufficient set of frame independent constitutive laws for isotropic rigid media is

$$\begin{aligned}
\hat{A} &= \hat{A}\left(\hat{\phi}, T\right) \\
\hat{S} &= \hat{S}(\hat{\phi}, T) \\
\mathbf{q} &= -k_{qT}(\hat{\phi}, T)\boldsymbol{\nabla} T - k_{q\phi}(\hat{\phi}, T)\boldsymbol{\nabla}\hat{\phi} \\
\mathbf{s} &= -k_{sT}(\hat{\phi}, T)\boldsymbol{\nabla} T - k_{s\phi}(\hat{\phi}, T)\boldsymbol{\nabla}\hat{\phi} \\
\boldsymbol{\phi} &= -k_{\phi T}(\hat{\phi}, T)\boldsymbol{\nabla} T - k_{\phi\phi}(\hat{\phi}, T)\boldsymbol{\nabla}\hat{\phi} \\
\hat{\sigma}_\phi &= \hat{\sigma}_\phi(\hat{\phi}, T)
\end{aligned}$$

which employ a "weak gradient" approximation and ensure that the vector fluxes vanish at equilibrium.

We assert that the specific free energy is,

$$\hat{A}\left(\hat{\phi}, T\right) = \hat{A}_S(T)\,\phi + \hat{A}_L(T)\,(1-\phi), \tag{4}$$

where $\phi = \frac{\hat{\phi}}{\hat{\phi}_{\max}}$ and $\hat{\phi}_{\max}$ is a maximum value of $\hat{\phi}$, $0 \leq \phi \leq 1$. Note that the media need not be pure crystal for $\phi = 1$. Adopting this simple assumption for $\hat{A}$ leads to the vector flux relations for $\mathbf{q}$ and $\boldsymbol{\phi}$ with clear physical interpretations (see Appendix A: Non Equilibrium Thermodynamics (NET) Model),

$$\mathbf{q} = -k_{qT}\boldsymbol{\nabla} T + k_{\phi\phi}\hat{L}\boldsymbol{\nabla}\phi \;;\; k_{qT} \geq 0 \tag{5}$$

$$\boldsymbol{\phi} = -k_{\phi\phi}\boldsymbol{\nabla}\hat{\phi} \tag{6}$$

where the cross-conductivity corresponding to thermal dispersion of ϕ, i.e. $k_{\phi T}$ is set to zero anticipating that the thermal dispersion effect is weak. Note that while the original vector constitutive laws resemble the linear phenomenological laws employed in conventional "irreversible" thermodynamics[24], symmetry among the conductivities k_{ij} does not apply here. The result for $\boldsymbol{\phi}$ indicates that $\hat{\phi}$ is transported by a dispersion effect and captures the physics of secondary nucleation. $k_{\phi\phi}$ is a dispersion coefficient between associated/solidifying segments and those in unattached chains in the disordered melt. Note that taking $k_{\phi\phi} = k_{\phi\phi}(\phi, T)$ allows modeling of the secondary nucleation as a dispersion mediated barrier crossing localized at the growth front (see section Including Interfacial Energy), as envisioned in recent work[7,11]. As a consequence of dispersion of ϕ, the latent heat $\hat{L} = \hat{U}_S(T) - \hat{U}_L(T)$ contributes to heat flux $\mathbf{q}$ just as the dispersion of components in a binary mixture does[24].

The second law also constrains the functional form for the specific rate of production $\hat{\sigma}_\phi(\hat{\phi}, T)$. At equilibrium $\hat{\sigma}_\phi(\hat{\phi}, T) \to 0$. Specifying $\hat{\phi} = 0$ for $T > T_m$ but $\hat{\phi} = \hat{\phi}_{\max}$ for $T < T_m$, $\hat{\sigma}_\phi(T, \hat{\phi})$ must have two roots $\hat{\phi} = \begin{pmatrix} 0 \\ \hat{\phi}_{\max} \end{pmatrix}$. The simplest positive definite functional form is quadratic in $\hat{\phi}$ (or equivalently in ϕ),

$$\hat{\sigma}_\phi(T, \hat{\phi}) = g(T)\phi(1-\phi) \tag{7}$$

The associated out of equilibrium rate of entropy production is

$$\Sigma_{\sigma_\phi} = -\frac{1}{T}\frac{\partial \hat{A}}{\partial \hat{\phi}}\rho\hat{\sigma}_\phi = \frac{\Delta\hat{S}_{\text{melt}}}{T\hat{\phi}_{\max}}(T_m - T)\rho\, g(T)\,\phi(1-\phi) \geq 0$$

where $\Delta\hat{S}_{melt}$ is the (positive) entropy of melting, and is obtained from Taylor expanding $\hat{A}_S(T) - \hat{A}_L(T)$ about the melting point T_m. Then, a simple form consistent with the second law is

$$\hat{\sigma}_\phi(T, \hat{\phi}) = R\hat{\phi}_{\max}\left(1 - \frac{T}{T_m}\right)\phi(1-\phi) \tag{8}$$

where R is a (positive) rate constant. When $T > T_m \Rightarrow \sigma_\phi(T, \hat{\phi}) < 0$ and the source term drives the system to the liquid state ($\hat{\phi} \to 0$); when $T < T_m \Rightarrow \sigma_\phi(T, \hat{\phi}) > 0$ and the source term drives the system to the solid state ($\hat{\phi} \to \hat{\phi}_{\max}$).

Combining the constitutive laws with the energy and internal variable balances leads to:

$$\rho\hat{C}\frac{\partial T}{\partial t} = \nabla\cdot(k_{qT}\nabla T) + \rho\hat{L}R\left(1 - \frac{T}{T_m}\right)\phi(1-\phi) \tag{9}$$

$$\rho\frac{\partial \phi}{\partial t} = \nabla\cdot(k_{\phi\phi}\nabla\phi) + \rho R\left(1 - \frac{T}{T_m}\right)\phi(1-\phi) \tag{10}$$

where $\hat{C}$ is the liquid state specific heat, and we have allowed for T and ϕ dependence of the transport coefficients. Equation 9 - 10 have the same structure as the corresponding one in Model A from the Ginzburg-Landau framework[22] although the physics underlying the second order terms differs: In equation 10, it accounts for dispersion of crystal nuclei by a gradient flux law, while in Model A it accounts for interfacial energy.

Before proceeding it is important to note the form of the "source" term in equation 10. In the Ginzburg-Landau formalism this corresponds to the (exchange) chemical potential. For materials that undergo gas-liquid coexistence there necessarily have to be three roots for the chemical potential, with two stable and one unstable root. The form of the source term that is used by us, on the other hand, has two roots, one stable and the other unstable as we have discussed above. Thus, while the Ginzburg-Landau formalism can resolve an intermediate composition by "phase separating" into the two stable equilibrium states, our formalism cannot. This fact must be remembered when we compare our results to those obtained using the classical approach, e.g., the work of Kobayashi[20].

3 Numerical solutions

To proceed further, the coupled differential equations 9-10 were solved numerically by the method of lines[25]. The second order terms on the right side of the equations are discretized using the

View Article Online
DOI: 10.1039/D6SM00323K

central difference approximation and the resulting coupled first order ordinary differential equations are solved by the implicit Euler method for the energy equation and the explicit Euler method for the solidification equation (see Appendix B: Numerical Methods for 1 and 2 Dimensional Calculations for details).

4 Application of NET Model to 1-D Solidification

We first consider one-dimensional solidification in an initially sub-cooled ($T = T_0 < T_m$) liquid ($\phi = 0$) domain, with instantaneous, heterogeneous primary nucleation at the left hand boundary (see Fig. 1).

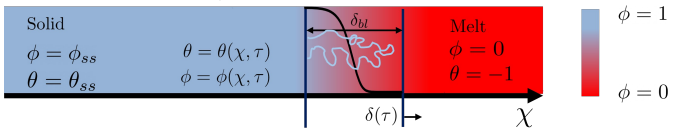

Fig. 1 Partially solidified 1-d domain $0 \le \chi \le l$ of initially sub-cooled liquid subject to heterogeneous primary nucleation at $\chi = 0,\ \tau = 0$.

4.1 Scaling

We non-dimensionalise equations 9- 10 using $\theta = \frac{T-T_m}{\Delta T}$, $\tau = tR\frac{\Delta T}{T_m}$ and $\chi = \frac{x}{\sqrt{\alpha/R\frac{\Delta T}{T_m}}}$ where $\Delta T = T_m - T_o$ is the undercooling, and $\alpha = \frac{k_{qT}}{\rho \hat{C}}$ is the thermal diffusivity:

$$\frac{\partial \theta}{\partial \tau} = \frac{\partial^2 \theta}{\partial \chi^2} - \lambda\, \theta\, \phi(1-\phi), \tag{11}$$

$$\frac{\partial \phi}{\partial \tau} = \beta\, \frac{\partial^2 \phi}{\partial \chi^2} - \theta\, \phi(1-\phi), \tag{12}$$

where the Stefan number $\lambda = \frac{\hat{L}}{\hat{C}\Delta T} \sim \mathscr{O}\left(10^0 - 10^1\right)$ for poly(ethylene oxide) near its melting point, and $\beta = \frac{k_{\phi\phi}}{\rho\alpha} \sim \mathscr{O}\left(10^{-3} - 10^{-2}\right)$. The characteristic time $1/R$ is related to the development of full crystallinity, and for polymer melts it should be of the order of the Rouse relaxation time at the entanglement threshold $\sim \mathscr{O}\left(10^{-6}\text{s}\right)$ [26]. Similarly, the characteristic length corresponds to the distance a thermal disturbance travels during $1/(R[\Delta T/T_m])$; this length is intermediate between the microscopic width of the growing crystal/melt interface and the spherulite size, and is $\sim \mathscr{O}(10^{-4} - 10^{-3}\text{cm})$. Thus, this model focuses on the larger interface between the melt and a fully-developed crystal, and not on the small length scales that are relevant to the lamellar (crystal)-amorphous interphase (i.e HL-stem length).

4.2 Equilibrium States

We perform a linear stability analysis of the model around the initial subcooled state. Consider weak disturbances of the form, $\theta(\chi,\tau) = -1 + \delta\theta\ ;\ 0 < \delta\theta << 1$ and $\phi(\chi,\tau) = \delta\phi\ ;\ 0 < \delta\phi << 1$. Then, the linearized dynamics of $\delta\phi$ are autonomous and obey

$$\frac{\partial}{\partial \tau}\delta\phi = \beta\frac{\partial^2}{\partial \chi^2}\delta\phi + \delta\phi$$

Using $\delta\phi(\chi,\tau) = \Phi_0 e^{iq_\phi \chi} e^{\Sigma_\phi \tau}$, we obtain the dispersion relation: $\Sigma_\phi = 1 - \beta q_\phi^2$. Thus, all Fourier modes for $q_\phi^2 < \frac{1}{\beta}$ are unstable. Moreover, the most susceptible mode is for $q_\phi \to 0$, indicating the absence of any pattern formation, and the resulting final states have uniform temperature and crystallinity.

The uniform final states of θ_{ss} and ϕ_{ss} are related by a global energy balance on the whole adiabatic domain and are independent of β:

$$\theta_{ss} + 1 = \lambda\, \phi_{ss}, \tag{13}$$

Thus, θ_{ss} and ϕ_{ss} are not independent, and the sensible heat in the final state derives entirely from latent heat release, Figs. 2(a) and 2(b). The particular equilibrium solutions do not span the entire $\theta_{ss} - \phi_{ss}$ domain, but are restricted to the boundaries, Fig. 2(a). The locus of all equilibrium solutions correspond to top (for $\lambda > 1$) and right hand (for $\lambda < 1$) boundary points of the (θ_{ss}, ϕ_{ss}). For $\lambda < 1$ the latent heat release is relatively weak, and not enough to heat the sub-cooled liquid to the melting point. Consequently the equilibrium state corresponds to a fully crystallized, subcooled solid: $\phi_{ss} = 1$, $\theta_{ss} + 1 = \lambda$. On the other hand when $\lambda > 1$ the opposite is true; the final state corresponds to partially crystallized material at the melting point: $\phi_{ss} = 1/\lambda$, $\theta_{ss} = 0$, that is, coexistence of liquid and solid at the melting point. The liquid-solid coexistence is expressed in the model as a uniform, intermediate value of $0 < \phi_{ss} < 1$. $\lambda = 1$ is the crossover between these two solutions Fig. 2(b).

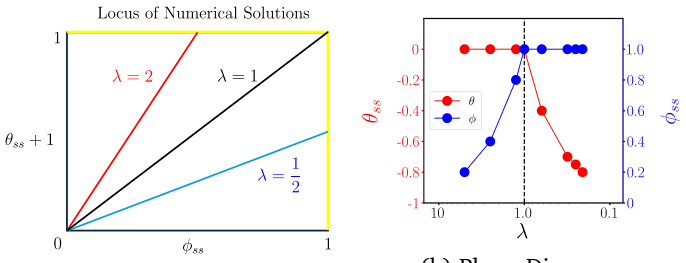

(a) Global Energy Balance (b) Phase Diagram

Fig. 2 (a) The global energy balance, equation 13, is shown in the $\theta_{ss} - \phi_{ss}$ plane as straight lines for various values of λ. The loci of steady-state solutions of the one-dimensional field equations on an adiabatic domain are shown as yellow lines. (b) The steady-state values (θ_{ss}, ϕ_{ss}) plotted against λ (independent of β), obtained from numerical solutions. For $\lambda < 1$, $\phi_{ss} = 1$ and $-1 < \theta_{ss} = \lambda - 1 < 0$ (sub-cooled solid), while for $\lambda > 1$, $\theta_{ss} = 0$ and $0 < \phi_{ss} = \frac{1}{\lambda} < 1$, corresponding to liquid–solid coexistence at T_m.

4.3 Traveling Waves

The results for various λ with β=0.1, Fig. 3, were derived using insulating conditions on both boundaries, with nucleation initiated at the left boundary. Following nucleation, there is a brief transient, but since the system is insulated, the thermal response

View Article Online
DOI: 10.1039/D6SM00323K

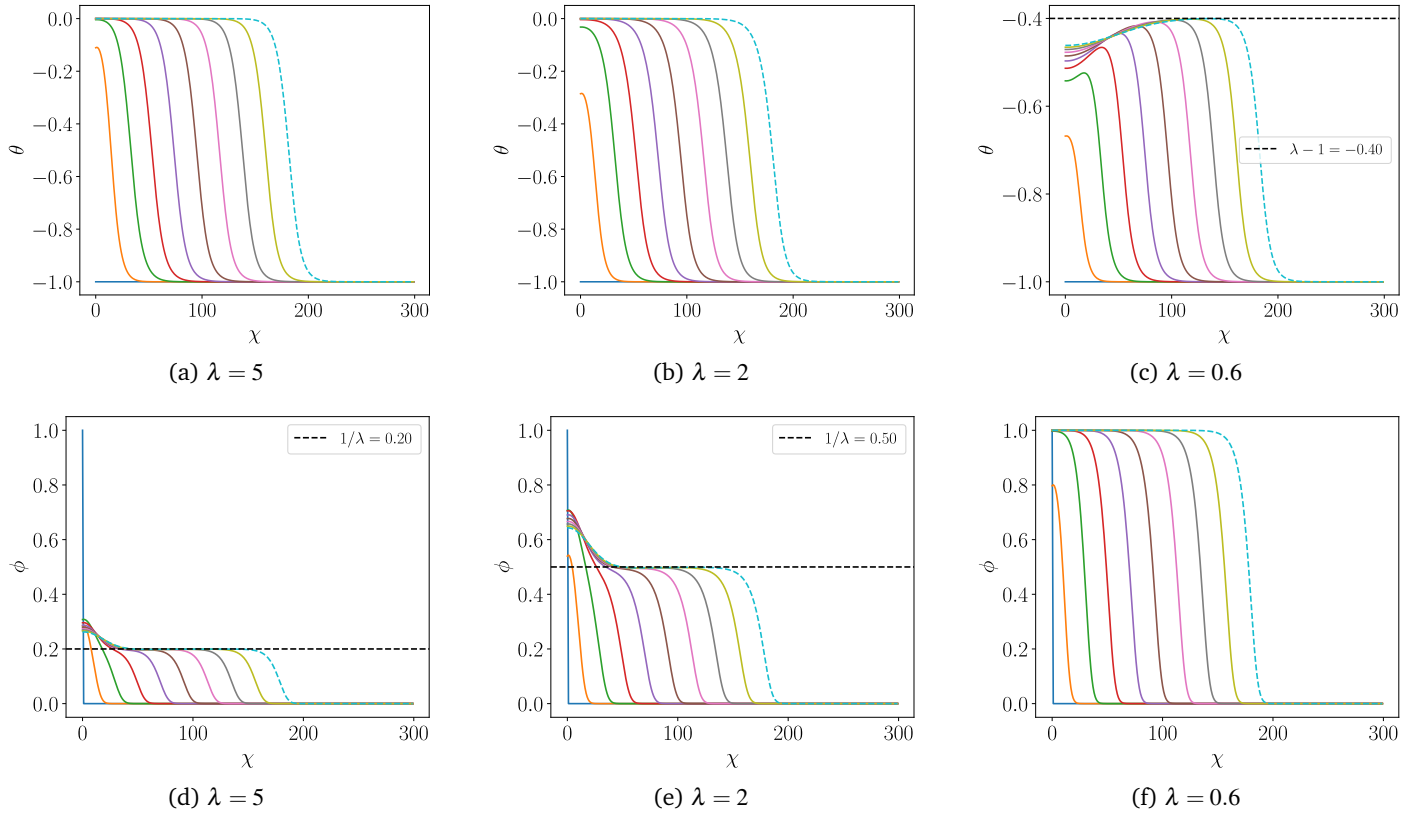

(a) $\lambda = 5$ (b) $\lambda = 2$ (c) $\lambda = 0.6$

(d) $\lambda = 5$ (e) $\lambda = 2$ (f) $\lambda = 0.6$

Fig. 3 The temperature profiles (θ) for the case (a) $\lambda = 5$, (b) $\lambda = 2$, (c) $\lambda = 0.6$ on a 1-d adiabatic domain after initial heterogeneous nucleation at the left. (d)-(f) Corresponding crystallinity (ϕ) profiles. In all cases $\beta = 0.1$. A propagating steady state front towards the right is obtained for longer times. The black dotted line in (d)-(e) is $\phi = 1/\lambda$. The black dotted line in (c) is $\lambda - 1$.

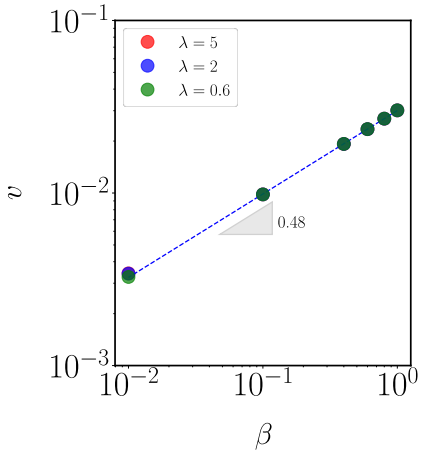

Fig. 4 The front propagation speed, υ vs. β, the constant slope indicates $\upsilon \sim \sqrt{\beta}$, and independent of λ.

is entirely due to latent heat release. Afterwards, sharp thermal and crystallinity traveling fronts emerge and move across the domain at constant speed. This follows since the equation governing ϕ is a Fisher-type, known to exhibit wave solutions[27–29]. For $\beta < 1$, the thermal front precedes the solidification front, regardless of λ. Remarkably, the fronts separate the sub-cooled liquid ahead of the front from material at the equilibrium state conditions, θ_{ss} and ϕ_{ss}, behind the front. That is, the traveling waves are adiabatic. We fit the instantaneous profiles with a hyperbolic tangent function with variable front position to determine the front speed, υ. By varying both β and λ two decades around characteristic values, we found that $\upsilon \sim \sqrt{\beta}$ independent of λ (Fig. 4). This observation reinforces that the dispersion term in the field equation for ϕ captures the physics of secondary nucleation. The relation $\upsilon \sim \sqrt{\beta}$ also results from a scaling argument. We assume that the ϕ profile has a characteristic interfacial thickness δ_ϕ. Asserting that the front advances $\sim \delta_\phi$ at the rate $\sim R' = R\frac{\Delta T}{T_m}$, then the characteristic (unscaled) velocity for this process is: $G \sim \delta_\phi R'$. Then, $\upsilon = \frac{G}{\sqrt{\alpha R'}} \sim \delta_\phi \sqrt{\frac{R'}{\alpha}}$. From the differential equation for ϕ the (scaled) layer thickness $\sim \sqrt{\beta}$, and thus, $\delta_\phi = \sqrt{\beta}\frac{\alpha}{R'}$. Consequently $\upsilon \sim \sqrt{\beta}$ consistent with numerical solutions.

View Article Online
DOI: 10.1039/D6SM00323K

4.4 Phase Space Analysis

We now proceed to perform a phase space analysis of the governing equations 11-12 in a frame of reference moving with the fronts $\eta = \chi - v\tau$, and assuming a steady state:

$$-v\frac{d}{d\eta}\theta = \frac{d^2}{d\eta^2}\theta - \lambda\theta\phi(1-\phi) \quad (14)$$

$$-v\frac{d}{d\eta}\phi = \beta\frac{d^2}{d\eta^2}\phi - \theta\phi(1-\phi) \quad (15)$$

where we leave v as an unknown. We take the auxiliary conditions to be $\lim_{\eta\to-\infty}\begin{pmatrix}\theta\\ \phi\end{pmatrix} = \begin{pmatrix}\theta_{ss}\\ \phi_{ss}\end{pmatrix}$, and $\lim_{\eta\to\infty}\begin{pmatrix}\theta\\ \phi\end{pmatrix} = \begin{pmatrix}-1\\ 0\end{pmatrix}$ where θ_{ss} and ϕ_{ss} are defined in equation 13. The equivalent fourth order autonomous system is

$$\begin{aligned}\frac{d\theta}{d\eta} &= u\\ \frac{du}{d\eta} &= \lambda\theta\phi(1-\phi) - vu\\ \frac{d\phi}{d\eta} &= \gamma\\ \frac{d\gamma}{d\eta} &= \frac{1}{\beta}\theta\phi(1-\phi) - \frac{v}{\beta}\gamma.\end{aligned} \quad (16)$$

Treating the two cases $\lambda > 1$ and $\lambda < 1$ separately, we find a pair of critical points for $(\theta_c, u_c, \phi_c, \gamma_c)$: $(0,0,1/\lambda,0)$ and $(-1,0,0,0)$ for $\lambda > 1$ and $(\lambda-1,0,1,0)$ and $(-1,0,0,0)$ for $\lambda < 1$. In both cases the first set corresponds to the left far-field conditions in real space, with the equilibrium values of θ_{ss} and ϕ_{ss} while the common second critical point corresponds to the right hand far field, the subcooled liquid. A linear stability analysis (see Appendix D: Phase Space Analysis of Steady Traveling Waves in 1 Dimension), indicates that the first are both unstable saddle points while the second critical point is a stable attractor iff $v \geq 2\sqrt{\beta}$. The last result reinforces that $v \sim \sqrt{\beta}$, as found numerically.

Fig. 5(a) and 5(b) show the spatial profiles of temperature θ and crystallinity ϕ for $\lambda = 5$ but for two different values of β. In both cases, the thermal front $\theta(\eta)$ travels just ahead of the solidification front $\phi(\eta)$, appears broader and is asymmetric with respect to the mean value of θ. The difference between $\theta(\eta)$ and $\phi(\eta)$ front shapes appears also in the phase space. Fig. 6 shows (i) u vs. θ and (ii) γ vs. ϕ cuts, displaying the trajectories in the phase space, that go from the left far-field (right-hand unstable critical point in Fig. 6) to right far-field (left-hand attractor in Fig. 6). These phase space trajectories have different shapes, with the u vs. θ plot skewed to the right relative to the nearly symmetric γ vs. ϕ cut, consistent with the real space profiles. These features are seen regardless of λ and for $\beta << 1$. The skewness in u vs. θ becomes more drastic for smaller β. Such plots reveal the $\theta(\eta)$ and $\phi(\eta)$ front shapes differ more drastically as β is reduced, reminiscent of profiles predicted by Stefan's moving boundary model[15].

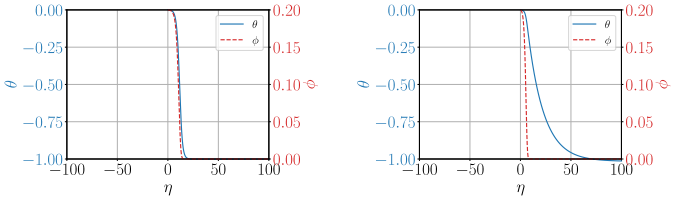

(a) $\lambda = 5.0$, $\beta = 0.1$ (b) $\lambda = 5.0$, $\beta = 0.001$

Fig. 5 Plots of θ and ϕ against η obtained from numerical solutions for $\lambda = 5$ and (a) $\beta = 0.1$ and (b) $\beta = 0.001$ by imposing $v = 2\sqrt{\beta}$. In both cases, the thermal front precedes the crystallinity front and is broader with considerable asymmetry.

4.5 Lovinger-Gryte Ansatz

Commonly, polymer crystallization experiments involve thermal quenching of the melt to a nominally uniform initial undercooling and subsequently tracking the solidification kinetics. An alternate protocol, zone annealing (ZA) or directional solidification, establishes a steady state by conveying the melt along a negative thermal gradient at constant speed V. In a frame moving with the melt, the media experiences a gradual thermal ramp into subcooled states where it solidifies. Lovinger and Gryte[18] carried out first such experiments on PEO melts to find unique oriented lamellar morphologies. These ZA experiments have been reproduced and broadened in scope recently[2,30]. By either protocol, the chain-folding process involved leaves a morphological signature of the effective undercooling during solidification: the lamellar long spacing decreases with undercooling. For the zone annealing process Lovinger and Gryte[18] posited that the effective undercooling corresponds to that for which the spherulite growth speed G matches V. Krauskopf *et al.*[30] recently verified this ansatz experimentally by comparing long spacings from PEO samples solidified by the two protocols. This analysis warrants a model prediction that the undercooling at the solidification front increases with front speed. Fig. 7 shows the representative numerical results for the scaled undercooling $-\theta_f$ at the solidification front, defined as $\phi = \frac{\phi_{ss}}{2}$, against scaled front speed v. The effective undercooling $-\theta_f$ increases linearly with v. This is consistent with the Lovinger-Gryte assumption.

5 Model Modifications

The previous section analyzed predictions for a simplified form of the model, *i.e.,* (i) the underlying intensive free energy, $\hat{A}(T,\phi)$, does not include interfacial energy (equation 4), (ii) the field equations (equations 9-10) are linearized with respect to temperature and (iii) the solidification process is one dimensional.

5.1 Including Interfacial Energy

It is now well-known, e.g., following the classic work of Poser-Sanchez[31], that the inclusion of gradient terms in the free energy expression captures the surface tension in the system. In our development, the free energy function accounts for variations in crystallinity and temperature, but does not account for changes in density across the solid-liquid boundaries, nor does it account for chain conformation variations across the crystal-amorphous inter-

View Article Online
DOI: 10.1039/D6SM00323K

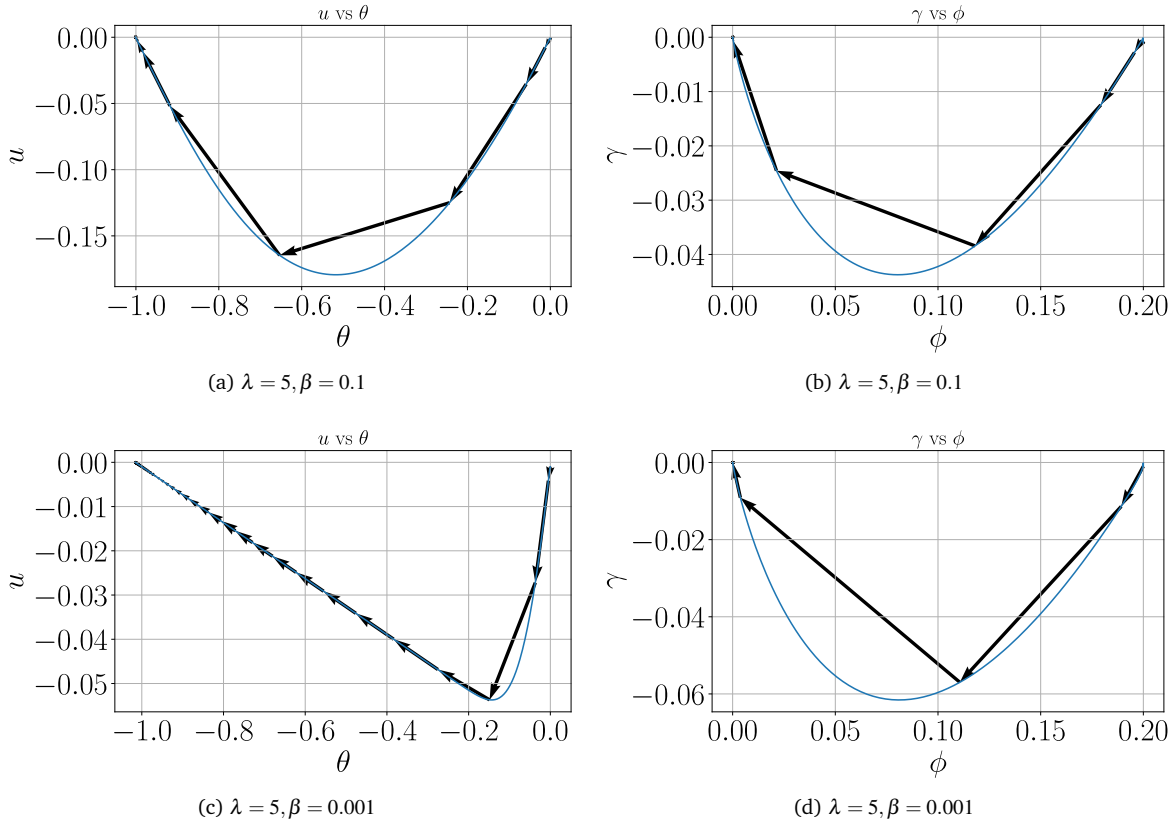

(a) $\lambda = 5, \beta = 0.1$ (b) $\lambda = 5, \beta = 0.1$

(c) $\lambda = 5, \beta = 0.001$ (d) $\lambda = 5, \beta = 0.001$

Fig. 6 Phase space plots: u vs. θ for $\lambda = 5$ for (a) $\beta = 0.1$, (c) $\beta = 0.001$, (b) & (d) corresponding γ vs. ϕ phase space plots.

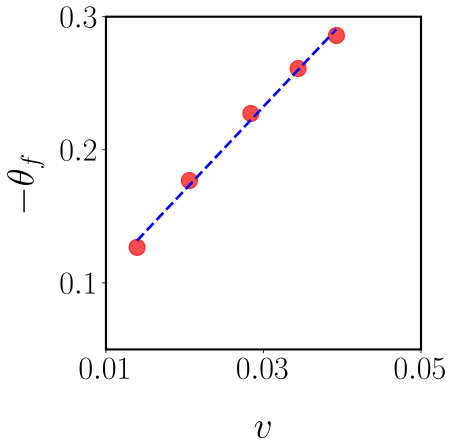

Fig. 7 Verification of Gryte-Lovinger hypothesis: effective undercooling, $-\theta_f$, calculated the solidification front where $\phi = \frac{\phi_{ss}}{2}$, against scaled front speed υ for $\lambda = 5$. The goodness of fit, $R^2 = 0.9949$.

phase. Clearly, the chain folding process, unique to the crystallization of flexible polymer melts, results in highly defected lamellar spherulite morphologies with significant interphase content. In fact the mean lamellar long-spacing l is an experimental measure inversely proportional to the specific interfacial area a_s of a fully solidified polymer. For semicrystalline polymers, the melting point T_m is suppressed systematically as l decreases. This is the Gibbs-Thomson effect[3]. The ribbon-like lamellae introduce considerable interfacial surface area, with associated interfacial energy $\gamma(T)$. We include this effect through an interfacial contribution to $\hat{A}(T, \phi)$:

$$\hat{A}\left(\hat{\phi}, T\right) = \hat{A}_L^{\infty}(T) + \left(\hat{A}_S^{\infty}(T) - \hat{A}_L^{\infty}(T)\right)\phi + \hat{A}_{int}(T, \phi) \tag{17}$$

where the superscript $^{\infty}$ indicates the bulk values, and $\hat{A}_{int}(T, \phi)$ is the interfacial contribution. If the semicrystalline morphology is scale-invariant, we can write

$$\hat{A}_{int}(T, \phi) = a_s \gamma(T) \phi, \tag{18}$$

This expression leads to a slightly revised specific rate of ϕ production, $\hat{\sigma}_{\phi}(T, \hat{\phi})$ (see Appendix E: Including Interfacial Energy in the NET Model)

$$\hat{\sigma}_{\phi}(T, \hat{\phi}) = R\hat{\phi}_{\max}\left[\left(1 - \frac{T}{T_m^{\infty}}\right) - \frac{\Gamma_s}{\Lambda}\right]\phi\,(1 - \phi) \tag{19}$$

View Article Online
DOI: 10.1039/D6SM00323K

where, $\Gamma_s \equiv \frac{a_s \gamma(T_m^\infty)}{T_m^\infty \Delta \hat{S}^\infty_{melt}(T_m^\infty)} > 0$, and $\Lambda = 1 + \frac{a_s \left(\frac{d\gamma}{dT}\right)_{T_m^\infty}}{\Delta \hat{S}^\infty_{melt}(T_m^\infty)} > 0$. Consequently, the effective melting point T_m corresponds to

$$\left(1 - \frac{T_m}{T_m^\infty}\right) - \frac{\Gamma_s}{\Lambda} = 0 \Rightarrow T_m = T_m^\infty \left(1 - \frac{\Gamma_s}{\Lambda}\right)$$

This is the Gibbs-Thomson relation which is consistent with experimental results on the melting behavior of semicrystalline polymers[3]. The corresponding (scaled) field equations using $\theta = \frac{T - T_m^\infty}{T_m^\infty - T_0} \equiv \frac{T - T_m^\infty}{\Delta T^\infty}$, $\chi = \frac{x}{\sqrt{\alpha / R \frac{\Delta T^\infty}{T_m^\infty}}}$, and $\tau = tR\frac{\Delta T^\infty}{T_m^\infty}$ are

$$\frac{\partial}{\partial \tau}\theta = \frac{\partial^2}{\partial \chi^2}\theta - \lambda\,(\theta + \gamma_s)\,\phi\,(1-\phi) \tag{20}$$

$$\frac{\partial}{\partial \tau}\phi = \beta \frac{\partial^2}{\partial \chi^2}\phi - (\theta + \gamma_s)\,\phi\,(1-\phi) \tag{21}$$

where $\gamma_s = \frac{\Gamma_s}{\Lambda}\frac{T_m^\infty}{\Delta T^\infty} > 0$. The effect of including interfacial energy is to suppress the effective melting point according to the Gibbs-Thomson rule, and consequently reduce the effective undercooling. The above equations exhibit traveling waves and correct equilibrium states, but with an effective melting point that is lower, as determined by l.

5.2 Including Barrier Crossing Kinetics and Molecular Weight Effects

Secondary nucleation controls the motion of the solidification front during polymer crystallization. Experimental, theoretical and computational studies[6–12], suggest that the secondary growth is a diffusion mediated barrier crossing process, i.e. a quasi-steady, non-linear dispersion process localized immediately at/ahead of the solidification front. The treatments mentioned, especially in Kundagrami and Muthukumar[9], suggest that the barrier results from the increased conformational entropy of chains partially incorporated into the solid at the front.

Let $c(x)$ be the number density of segments of partially included chains in a one dimensional, steady process. In this case, the constant number flux $j\ [=]\ \frac{\#}{L^2 T}$ near the solidification front obeys

$$j = -D(T,c)\frac{\partial}{\partial x}c - \frac{c}{f}\frac{\partial}{\partial x}\Psi(x) \tag{22}$$

where $D(T,c)$ is a segment diffusivity, $f\ [=]\ \frac{ET}{\#L^2}$ is the segment friction coefficient, and $\Psi(x)\ [=]\ \frac{E}{\#}$ is the potential per segment describing the self-generated free energy barrier near the front. Multiplying through by the segment volume b^3 produces the front speed $b^3 j = G$ and the replacement $b^3 c = \phi$. If $\phi(x)$ is a monotonic function, then $\phi^{-1}(x) \to x(\phi)$, and one can write $\frac{\partial}{\partial x}\Psi(x) = \frac{d}{d\phi}\psi(\phi)\frac{\partial}{\partial x}\phi$ to describe the rate of secondary nucleation as a dispersion process

$$G = -D_{eff}(T,\phi)\frac{\partial}{\partial x}\phi \tag{23}$$

with an effective diffusivity,

$$D_{\text{eff}}(T,\phi) = D - \frac{\phi}{f}\frac{d\psi(\phi)}{d\phi} = \frac{k_{\phi\phi}(T,\phi)}{\rho} \tag{24}$$

Because of the barrier term, $\frac{k_{\phi\phi}}{\rho}$ can exhibit a severe, typically exponential, temperature dependence [see Hoffman *et al.* for example, where $G \sim \exp\left(-\frac{B}{T_m - T_0}\right)$ for relatively small undercoolings].

In the analysis described earlier (section Application of NET Model to 1-D Solidification), the scaled dispersion term representing the rate of secondary nucleation, the first term on the right in equation 12, was linearized and β, the scaled dispersion coefficient, was taken as a constant. Interestingly, these assumptions produce the spurious result that $v \sim \sqrt{\beta}$, independent of the undercooling, $T_m - T_0 = \Delta T_0$. This is certainly inconsistent with experimental results, but can be easily remedied now with no thermodynamic contradiction by the replacement $\beta \frac{\partial^2}{\partial \chi^2}\phi \to \frac{\partial}{\partial \chi}\beta(\theta)\frac{\partial}{\partial \chi}\phi$ where $\beta(\theta)$ has a θ dependence consistent with barrier crossing. For example taking $\beta(\theta) = \beta_0 \exp\left(\frac{B}{\theta \Delta T_0}\right)$ with $\beta(\theta_f) << 1$ gives a field equation for ϕ with a non-linear dispersion term, predicting sharp traveling fronts, correct equilibrium states, a front speed depending on undercooling consistent with experiment for small undercoolings, and consistent with the Gryte-Lovinger ansatz as shown in Fig. 8(d). The morphology of semicrystalline polymers is indeed controlled by entanglements, and the recent work of Thurn-Albrecht[32] and coworkers shows that, while the crystal thickness only depends on supercooling, the amorphous phase thickness is proportional to the entanglement density. While these are important points, our model is operative on a much coarser (μm) length scale. Thus, such details are not captured in our model and are not the focus of our current work. Additionally, the growth rate for crystals appears to be strongly dependent on molecular weight[33,34], especially below the entanglement threshold. While this effect can be captured by making the parameter β molecular weight dependent in the growth kinetics equation, this is beyond the scope of this manuscript.

6 Two Dimensional Systems

Consistent with analysis on one-dimension done so far, we now show that sharp thermal and solidification fronts also emerge and travel at constant speed in two dimensions. For this purpose we carry out two dimensional simulations, initialized with a narrow solid cylindrical "post" exposed to the subcooled liquid, but insulated thereafter. The calculations use the linearized model, yet demand a more sophisticated numerical scheme (a hybrid implicit/explicit algorithm was used, see Appendix B: Numerical Methods for 1 and 2 Dimensional Calculations).

Figs. 9(a) and 9(b) illustrate the results, with "heat maps" and profiles along 1-d horizontal cuts of $\theta(\chi,\zeta,\tau)$ and $\phi(\chi,\zeta,\tau)$ in an insulated square domain after a primary nucleation at the center. Sharp thermal and solidification fronts emerge during a transient and eventually travel radially outward together *at constant speed* (see Fig. 9(b)) with no indication of front instabilities (e.g. Mullins Sekerka instability) for the range of parameters explored ($0.01 \le \beta \le 0.1$; $\lambda = 0.5$ and 1.5). The model predicts that

View Article Online
DOI: 10.1039/D6SM00323K

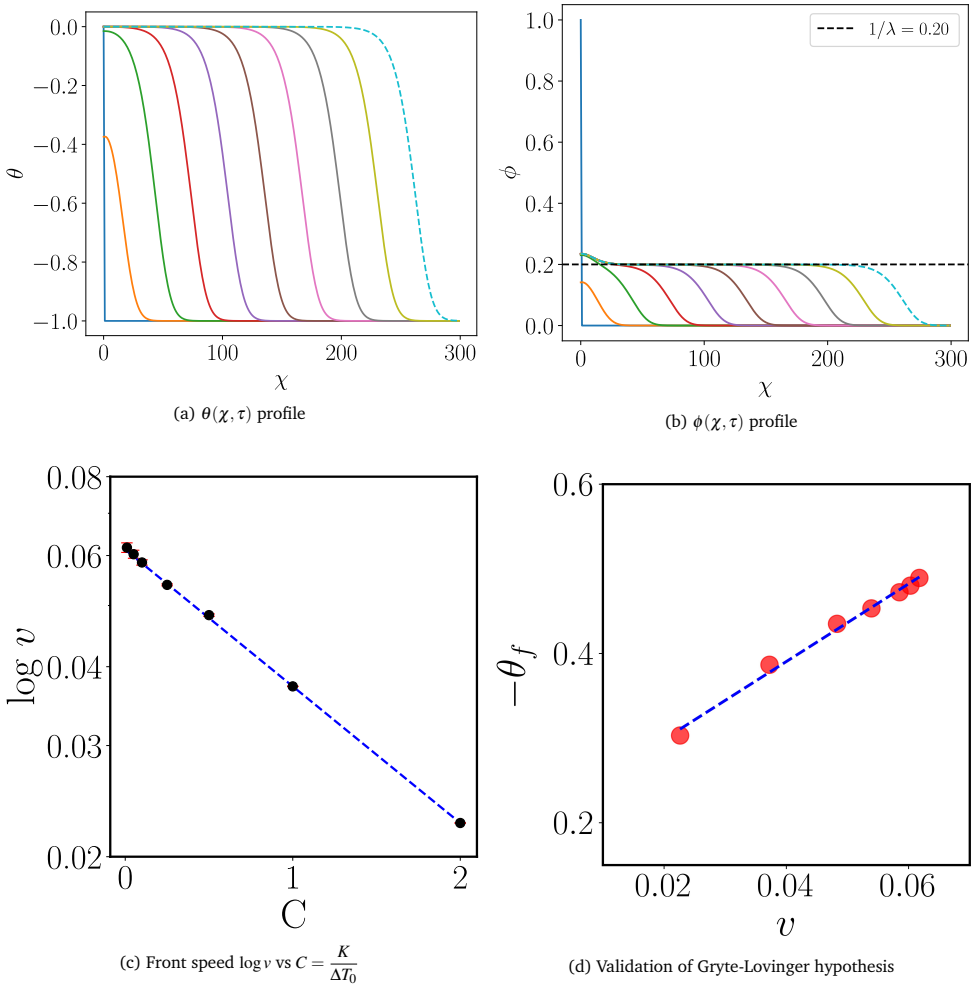

(a) $\theta(\chi,\tau)$ profile

(b) $\phi(\chi,\tau)$ profile

(c) Front speed $\log v$ vs $C = \frac{K}{\Delta T_0}$

(d) Validation of Gryte-Lovinger hypothesis

Fig. 8 (a)-(b) $\theta(\chi,\tau)$ and $\phi(\chi,\tau)$ profiles with the non-linear dispersion term (equation 24) for $\beta_0 = 1.0$, $C = 0.5$, and $\lambda = 5$. (c) Front speed with nonlinear dispersion consistent with L-H kinetics; $\log v$ vs $C = \frac{K}{\Delta T_0}$ for $\beta_0 = 1.0$, $\lambda = 5$. Note $\beta_f = \beta(\theta_f) \ll 1$ in all cases with $v \sim \sqrt{\beta_f}$ for fixed λ. (d) Validation of Gryte-Lovinger hypothesis: $-\theta_f$ vs v from the model using the nonlinear dispersion term, consistent with data from panel (a).

polymer spherulites grow in two dimensions as geometric objects rather than develop into dendritic structures, in agreement with the preponderance of extant experiment.

7 Summary and Conclusions

We developed a non-equilibrium thermodynamic model for solidification, which enforces non-negative rates of entropy production locally, and applied it to subcooled polymer melts. The formulation yields coupled balance equations for the thermal energy and extent of solidification, ϕ, resembling a nonlinear diffusion-reaction system. The equation for ϕ is a Fisher type and includes a dispersion term accounting for secondary nucleation. The overall structure of the model is remarkably similar to model A for a scalar order parameter ϕ in the Ginzberg-Landau framework, (see Kobayashi, for example). However the physics underlying the dispersion and source terms for ϕ are different in the two models: In the phase field approach the second order term accounts for interfacial free energy and together with its source permits inhomogeneous equilibrium states, in contrast to the thermodynamic model here. In its simplest form, the current model, linearized with respect to temperature, has two dimensionless parameters λ and β. λ is the Stefan number, expected to be $\mathcal{O}(10^0 - 10^1)$, giving the latent heat relative to the sensible heat to the melting point. β is the dispersion coefficient for ϕ scaled by the thermal dispersion coefficient, expected to be $\mathcal{O}(10^{-3} - 10^{-1})$.

The NET model properly describes real polymer solidification. For realistic values of λ and β the model predicts sharp solidification and thermal fronts traveling together at constant speed. The solidification fronts conform to a symmetric hyperbolic tangent function while the thermal fronts precede those for ϕ and are broader and asymmetric with an extended "foot" into the melt, the feature becoming more extreme as β is reduced, reminiscent of Stefan model solutions. For constant β the front speed scales $v \sim \sqrt{\beta}$, anticipated by a simple scaling argument presuming the rate of solidification at the front controls its motion, and verified mathematically by a phase space analysis.

For adiabatic systems, the model predicts uniform equilibrium states consistent with the phase diagram expected based on the prescribed specific free energy $\hat{A}(\theta,\phi)$. These states are independent of the kinetic parameter β and controlled by λ. If the $\lambda < 1$ a

View Article Online
DOI: 10.1039/D6SM00323K

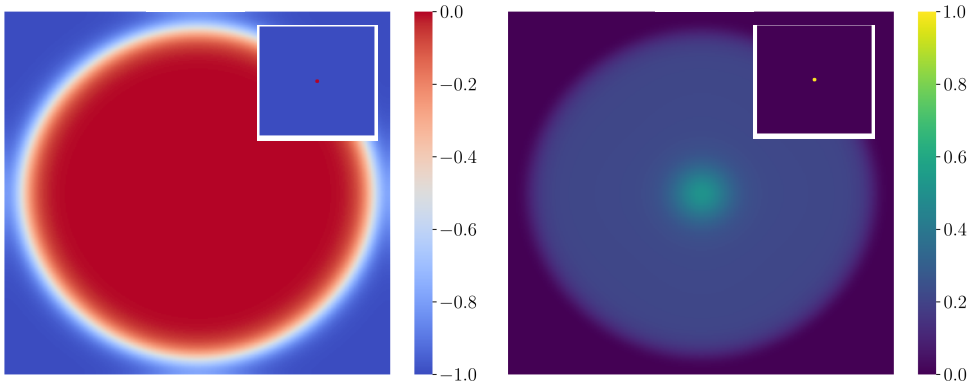

(a) "Heat maps" showing $\theta(\chi,\zeta,\tau>0)$ (left) and $\phi(\chi,\zeta,\tau>0)$ (right) in an insulated square domain following a central heterogeneous primary nucleation according to the linearized model for $\beta=0.1$ and $\lambda=5$.

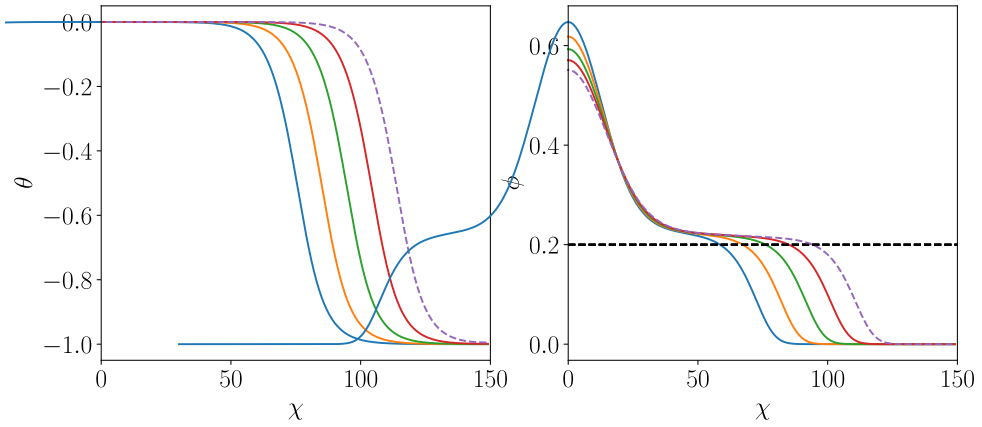

(b) $\theta(\chi,\zeta=0,\tau>0)$ and $\phi(\chi,\zeta=0,\tau>0)$ profiles along a horizontal cut through the origin for the system in panel (a). The front profiles resemble those for a 1-d system: adiabatic traveling waves develop after nucleation, moving radially outward at constant speed.

Fig. 9 Two-dimensional temperature and crystallinity profiles. Panel (a) shows the full 2D heat maps of θ and ϕ, while panel (b) shows horizontal cut profiles through the origin.

subcooled, fully solidified material results ($\phi_{ss}=1$, $-1<\theta_{ss}<0$). If $\lambda>1$ "mushy", partially solidified material results ($0<\phi_{ss}<1$, $\theta_{ss}=0$), that is solid in equilibrium with disordered material.

The most common experimental methods for tracking melt crystallization kinetics monitor the *overall* extent of crystallization as a function of time. This is proportional to $\bar{\phi}(\tau)=\frac{1}{\mathscr{V}}\int\phi(\chi,\tau)d\chi$, where $\mathscr{V}$ is the sample volume and χ is position in the sample. Such data are typically rescaled to range from 0 to 1 to yield $\Phi(\tau)$ say. Experimental plots of $\Phi(\tau)$ vs. τ show a characteristic sigmoidal shape and are typically fit with the semi-empirical Avrami equation $\Phi(\tau)=1-e^{-K\tau^n}$ where K and n (the "Avrami constants") depend on the front speed characteristics and mode of primary nucleation. Some specific results for K and n are known from mean field treatments of the kinetics (see Lodge). For example, if it be randomly placed, instantaneous, (heterogeneous) primary nucleation of solid discs growing at constant rate in two dimensions, then $n=2$, while if the front speed be diffusion controlled ($G\sim 1/\sqrt{t}$) then $n=1$. It is relatively straightforward to simulate this 2-d process with our model. We use a constant scaled dispersion coefficient β, which does not include interfacial tension contributions. Fig. 10 shows an example, using "heat maps", for twenty randomly placed initial nucleation sites in a square, insulated domain. The resulting partially developed solid morphology $\phi(\chi,\zeta,\tau>0)$ strongly resembles experimental optical microscopy images of the same (see Fig. 11 and Lodge, for example). A plot of $\Phi(\tau)$ vs τ for the calculations in Fig. 10, exhibits a sigmoidal shape. A two parameter regression fit to the Avrami equation (Fig. 10) gives $n=1.42$, between the values of $n=1$ and $n=2$ anticipated by the estimates above. For this simulation the influence of the initial diffusion controlled transients immediately following primary nucleation evidently influences the Avrami fitting results. In the future we plan to undertake more detailed comparisons between this model and closely related phase-field models, as well as application to directional solidification and melting.

View Article Online
DOI: 10.1039/D6SM00323K

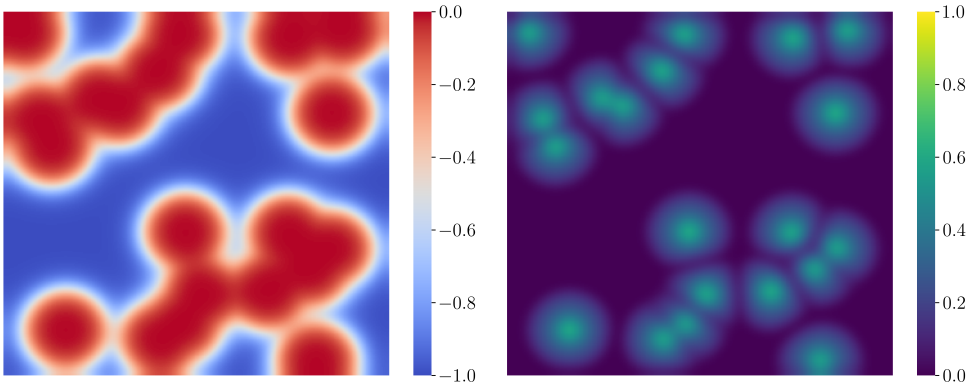

(a) Heat maps showing $\theta(\chi,\zeta,\tau>0)$ and $\phi(\chi,\zeta,\tau>0)$ in an insulated square domain following instantaneous heterogeneous primary nucleation at twenty randomly placed sites for $\beta=0.1$ and $\lambda=5$.

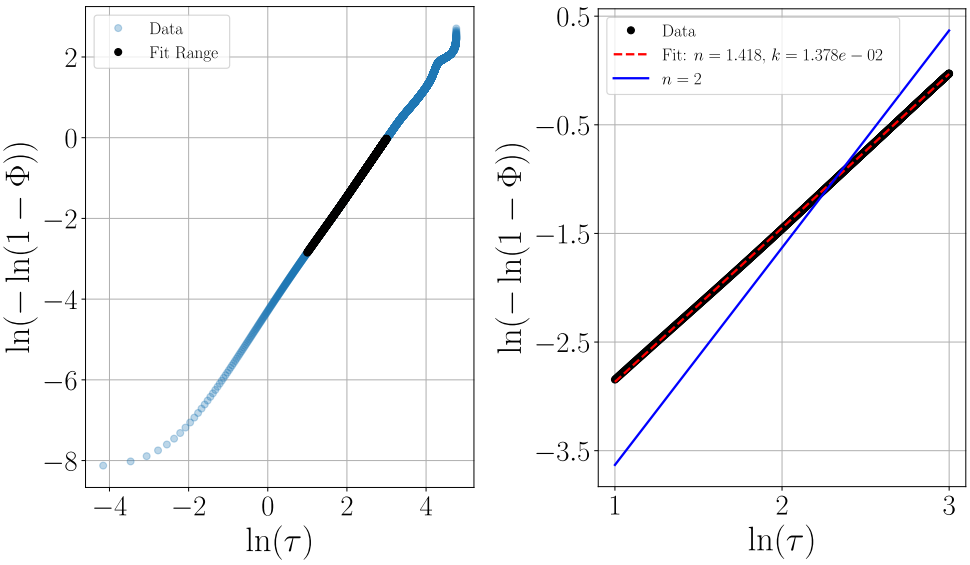

(b) Avrami fit

(c) Avrami fit: zoomed/fitted segment

Fig. 10 (a) Heat maps showing θ and ϕ in a 2D domain with multiple nucleation sites; adiabatic traveling waves develop radially outward, forming polygonal final spherulite boundaries. (b)-(c) Avrami fits for the 2D simulations in (a); (c) is a zoomed-in segment of (b).

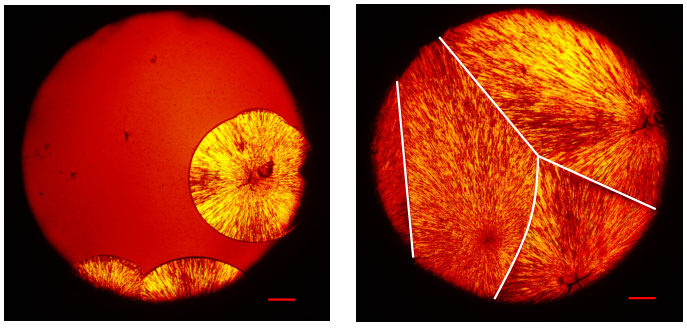

(a) Initial morphology (b) Final morphology

Fig. 11 Polarized light optical microscopy (PLOM) images of poly(ethylene oxide) (PEO) melt crystallizing at 53.1 °C. The scale bar corresponds to 200 μm. The final morphology (b) shows the impinged spherulitic borders in white.

A Appendix A: Non Equilibrium Thermodynamics (NET) Model

The following development draws on methods developed in Müller. Consider isotropic rigid media with the density ρ fixed. The media's local non-equilibrium state depends on the temperature and an intensive, frame-indifferent scalar "internal variable" or order parameter $\hat{\phi}\left(\hat{\phi}\,[=]\,\frac{1}{M}\right)$ which obeys a balance law

$$\rho\frac{\partial}{\partial t}\hat{\phi}+\boldsymbol{\nabla}\cdot\boldsymbol{\phi}-\rho\sigma_{\phi}=0$$

where $\boldsymbol{\phi}$ and σ_{ϕ} are the local conductive flux and production density of $\hat{\phi}$, respectively. This could be, for example, the fraction per unit mass of solid in a solid/liquid mixture, both modeled as rigid (motionless) media. The primary fields are the internal variable and temperature, $\hat{\phi}(\mathbf{r},t)$ and $T(\mathbf{r},t)$, governed by the above equa-

View Article Online
DOI: 10.1039/D6SM00323K

tion and the energy balance

$$\rho \frac{\partial}{\partial t}\hat{U} + \boldsymbol{\nabla}\cdot\mathbf{q} = 0$$

and subject to the second law

$$\rho \frac{\partial}{\partial t}\hat{S} + \boldsymbol{\nabla}\cdot\mathbf{s} \geq 0$$

where $\hat{U},\mathbf{q},\hat{S},\mathbf{s}$ are the non-equilibrium (local valued) specific internal energy, conductive energy flux, specific entropy, and conductive entropy flux, respectively. The temperature field T appears implicitly in the above; for example, the local internal energy must depend on the local temperature. To ensure that T has the usual significance at equilibrium, we include the relation

$$\hat{A} = \hat{U} - T\hat{S}$$

where $\hat{A}$ is the local specific free energy out of equilibrium. This defines the local non-equilibrium temperature.

We can determine the degrees of freedom (DOF) in the above framework. With 3 equations (two scalar balances and a definition of T) to find 15 unknown functions $(\hat{\phi},\boldsymbol{\phi},\sigma_\phi,\hat{U},\mathbf{q},\hat{S},\mathbf{s},\hat{A},T)$ one has 12 DOF.

The DOF can be satisfied by proposing a sufficient set of constitutive laws

$$\begin{aligned}
\hat{A} &= \hat{A}(\ldots)\\
\hat{S} &= \hat{S}(\ldots)\\
\sigma_\phi &= \sigma_\phi(\ldots)\\
\boldsymbol{\phi} &= \boldsymbol{\phi}(\ldots)\\
\mathbf{q} &= \mathbf{q}(\ldots)\\
\mathbf{s} &= \mathbf{s}(\ldots)
\end{aligned}$$

where $(\ldots)$ are derived from $\hat{\phi}(\mathbf{r},t')$ and $T(\mathbf{r},t')$ for $-\infty < t' \leq t$. If one assumes that only the current local state matters, one can write down a set of "linearized" (i.e. "weak gradient") frame indifferent constitutive laws for this class of materials:

$$\begin{aligned}
\hat{A} &= \hat{A}(\hat{\phi},T)\\
\hat{S} &= \hat{S}(\hat{\phi},T)\\
\mathbf{q} &= -k_{qT}(\hat{\phi},T)\boldsymbol{\nabla}T - k_{q\phi}(\hat{\phi},T)\boldsymbol{\nabla}\hat{\phi}\\
\mathbf{s} &= -k_{sT}(\hat{\phi},T)\boldsymbol{\nabla}T - k_{s\phi}(\hat{\phi},T)\boldsymbol{\nabla}\hat{\phi}\\
\boldsymbol{\phi} &= -k_{\phi T}(\hat{\phi},T)\boldsymbol{\nabla}T - k_{\phi\phi}(\hat{\phi},T)\boldsymbol{\nabla}\hat{\phi}\\
\sigma_\phi &= \sigma_\phi(\hat{\phi},T)
\end{aligned}$$

Adopt a weak assumption that $\hat{A} = \hat{A}\left(\hat{\phi},T\right)$ has the same functional relationship with T as at equilibrium; consequently $\left(\frac{\partial \hat{A}}{\partial T}\right) = -\hat{S}$. One can then apply Liu's theorem (see Müller) to determine the constraints on the above constitutive functions imposed by the second law. One first creates an "augmented" inequality by adding the balance laws as constraints, each multiplied by a Lagrange multiplier:

$$\rho \frac{\partial}{\partial t}\hat{S} + \boldsymbol{\nabla}\cdot\mathbf{s} - \Lambda^\phi\left(\rho\frac{\partial}{\partial t}\hat{\phi} + \boldsymbol{\nabla}\cdot\boldsymbol{\phi} - \sigma_\phi\right) - \Lambda^T\left(\rho\frac{\partial}{\partial t}\hat{U} + \boldsymbol{\nabla}\cdot\mathbf{q}\right) \geq 0$$

Then, inserting the constitutive laws, the definition of T, and applying the chain rule leads to

$$\begin{aligned}
&\rho\left[\left(1-\Lambda^T T\right)\frac{\partial \hat{S}}{\partial T} - \Lambda^T\left(\frac{\partial \hat{A}}{\partial T} + \hat{S}\right)\right]\frac{\partial T}{\partial t}\\
&+\rho\left[\frac{\partial \hat{S}}{\partial \hat{\phi}} - \Lambda^T\left(\frac{\partial \hat{A}}{\partial \hat{\phi}} + T\frac{\partial \hat{S}}{\partial \hat{\phi}}\right) - \Lambda^\phi\right]\frac{\partial \hat{\phi}}{\partial t}\\
&+\left[\Lambda^T k_{qT} + \Lambda^\phi k_{\phi T} - k_{sT}\right]\nabla^2 T\\
&+\left[\Lambda^T k_{q\phi} + \Lambda^\phi k_{\phi\phi} - k_{s\phi}\right]\nabla^2\hat{\phi}\\
&+\nabla T\cdot\left(\Lambda^T\nabla k_{qT} + \Lambda^\phi\nabla k_{\phi T} - \nabla k_{sT}\right)\\
&+\nabla\hat{\phi}\cdot\left(\Lambda^T\nabla k_{q\phi} + \Lambda^\phi\nabla k_{\phi\phi} - \nabla k_{s\phi}\right)\\
&+\Lambda^\phi\sigma_\phi \geq 0
\end{aligned} \tag{25}$$

In the context of Liu's theorum, $X_\gamma = \left(\frac{\partial T}{\partial t}, \frac{\partial \hat{\phi}}{\partial t}, \nabla^2 T, \nabla^2\hat{\phi}\right)$. In so far as $\hat{\phi}(\mathbf{r},t)$ and $T(\mathbf{r},t)$ can be considered arbitrary and independent (i.e. unconstrained by the balance laws), the X_γ can be considered arbitrary and independent, and since they appear linearly in the augmented inequality, the bracketed quantities in the first four terms must vanish. Using the assumption $\left(\frac{\partial \hat{A}}{\partial T}\right) = -\hat{S}$ the first term gives

$$\Lambda^T = \frac{1}{T}$$

The second term vanishing then gives

$$\frac{\partial \hat{A}}{\partial \hat{\phi}} = -\frac{\Lambda^\phi}{\Lambda^T} = -T\Lambda^\phi \Rightarrow \Lambda^\phi = -\frac{1}{T}\frac{\partial \hat{A}}{\partial \hat{\phi}}$$

The third and fourth terms vanishing lead to

$$\begin{aligned}
k_{sT} &= \frac{1}{T}k_{qT} + \Lambda^\phi k_{\phi T}\\
k_{s\phi} &= \frac{1}{T}k_{q\phi} + \Lambda^\phi k_{\phi\phi}
\end{aligned}$$

View Article Online
DOI: 10.1039/D6SM00323K

which implies

$$\mathbf{s} = \frac{1}{T}\mathbf{q} + \Lambda^{\phi}\boldsymbol{\phi} = \frac{1}{T}\mathbf{q} - \frac{1}{T}\frac{\partial \hat{A}}{\partial \hat{\phi}}\boldsymbol{\phi}$$

One can then show from the conditions determined above, the following inequality still needs to be satisfied

$$\Sigma \equiv A_{TT}(\nabla T)^2 + A_{\phi T}\left(\nabla\hat{\phi}\cdot\nabla T\right) + A_{\phi\phi}\left(\nabla\hat{\phi}\right)^2 + B\sigma_{\phi} \geq 0$$

where

$$\begin{aligned} A_{TT} &= \left(\frac{k_{qT}}{T^2} - \frac{k_{\phi T}}{T^2}\frac{\partial \hat{U}}{\partial \hat{\phi}}\right) \\ A_{\phi T} &= \left(\frac{k_{q\phi}}{T^2} - \frac{k_{\phi\phi}}{T^2}\frac{\partial \hat{U}}{\partial \hat{\phi}} + \frac{k_{\phi T}}{T}\frac{\partial^2 \hat{A}}{\partial \hat{\phi}^2}\right) \\ A_{\phi\phi} &= \frac{k_{\phi\phi}}{T}\frac{\partial^2 \hat{A}}{\partial \hat{\phi}^2} \\ B &= -\frac{1}{T}\frac{\partial \hat{A}}{\partial \hat{\phi}} \end{aligned}$$

To ensure this "residual" inequality is satisfied one can apply the criteria that Σ is a minimum at equilibrium, where gradients vanish, i.e. for the minimization of Σ wrt $Y_\alpha = \left(\frac{\partial T}{\partial x_i}, \frac{\partial \hat{\phi}}{\partial x_i}\right)$, namely

$$\left.\frac{\partial \Sigma}{\partial Y_\alpha}\right|_{Y_\beta = 0} = 0$$

$$\left\| \frac{\partial^2 \Sigma}{\partial Y_\alpha \partial Y_\beta} \right\|_{Y_\gamma = 0} \text{ non-negative}$$

If we simplify to a $1-d$ system then

$$\Sigma \equiv A_{TT}\left(\frac{\partial T}{\partial x}\right)^2 + A_{\phi T}\left(\frac{\partial \hat{\phi}}{\partial x}\frac{\partial T}{\partial x}\right) + A_{\phi\phi}\left(\frac{\partial \hat{\phi}}{\partial x}\right)^2 + B\sigma_{\phi} \geq 0$$

The first criterion is identically satisfied. The Hessian is

$$\mathbf{H} = \begin{bmatrix} A_{TT} & A_{\phi T} \\ A_{\phi T} & A_{\phi\phi} \end{bmatrix}$$

and positive definite iff

$$\begin{aligned} Tr\mathbf{H} &\geq 0 \\ \det\mathbf{H} &\geq 0 \end{aligned}$$

or

$$\begin{aligned} A_{TT} + A_{\phi\phi} &\geq 0 \\ A_{TT}A_{\phi\phi} - A_{\phi T}^2 &\geq 0 \end{aligned}$$

Now for crystallization, a reasonable assertion is

$$\begin{aligned} \hat{A}\left(\hat{\phi}, T\right) &= \hat{A}_S(T)\,\phi + \hat{A}_L(T)\,(1-\phi), \quad \phi = \frac{\hat{\phi}}{\hat{\phi}_{\max}} \\ &= \hat{A}_L(T) + \left(\hat{A}_S(T) - \hat{A}_L(T)\right)\phi \end{aligned}$$

where $\hat{\phi}_{\max}$ is a maximum value of $\hat{\phi}$, and the subscripts indicate the phase (S for solid and L for liquid). Then

$$\frac{\partial \hat{A}}{\partial \hat{\phi}} = \frac{\hat{A}_S}{\hat{\phi}_{\max}}(T) - \frac{\hat{A}_L}{\hat{\phi}_{\max}}(T) \equiv \frac{1}{\hat{\phi}_{\max}}\left(\hat{A}_S(T) - \hat{A}_L(T)\right)$$

Further

$$\frac{\partial^2 \hat{A}}{\partial \hat{\phi}^2} = 0$$

and

$$\begin{aligned} A_{TT} &= \left(\frac{k_{qT}}{T^2} - \frac{k_{\phi T}}{T^2}\frac{\partial \hat{U}}{\partial \hat{\phi}}\right) \\ A_{\phi T} &= \left(\frac{k_{q\phi}}{T^2} - \frac{k_{\phi\phi}}{T^2}\frac{\partial \hat{U}}{\partial \hat{\phi}}\right) \\ A_{\phi\phi} &= 0 \end{aligned}$$

simplifying the minimization criteria to

$$\begin{aligned} A_{TT} &= \left(\frac{k_{qT}}{T^2} - \frac{k_{\phi T}}{T^2}\frac{\partial \hat{U}}{\partial \hat{\phi}}\right) \geq 0 \\ A_{\phi T} &= \left(\frac{k_{q\phi}}{T^2} - \frac{k_{\phi\phi}}{T^2}\frac{\partial \hat{U}}{\partial \hat{\phi}}\right) = 0 \end{aligned}$$

The last indicates

$$k_{q\phi} = k_{\phi\phi}\frac{\partial \hat{U}}{\partial \hat{\phi}} = \frac{k_{\phi\phi}}{\hat{\phi}_{\max}}\left(\hat{U}_S(T) - \hat{U}_L(T)\right) = -\frac{k_{\phi\phi}}{\hat{\phi}_{\max}}\hat{L}$$

If we set the cross-coefficient $k_{\phi T} = 0$ then we have the second law requirement $k_{qT} \geq 0$ and the flux relations are

$$\begin{aligned} \mathbf{q} &= -k_{qT}\nabla T + \frac{k_{\phi\phi}}{\hat{\phi}_{\max}}\hat{L}\nabla\hat{\phi} \\ \boldsymbol{\phi} &= -k_{\phi\phi}\nabla\hat{\phi} \end{aligned}$$

and the balance laws are

$$\begin{aligned} \rho\frac{\partial}{\partial t}\hat{U} + \boldsymbol{\nabla}\cdot\mathbf{q} &= \rho\frac{\partial}{\partial t}\left(\hat{U}_L(T) - \hat{L}\phi\right) + \boldsymbol{\nabla}\cdot\mathbf{q} = 0 \\ \rho\hat{C}\frac{\partial}{\partial t}T &= k_{qT}\nabla^2 T - \frac{k_{\phi\phi}}{\hat{\phi}_{\max}}\hat{L}\nabla^2\hat{\phi} + \rho\frac{\hat{L}}{\hat{\phi}_{\max}}\frac{\partial}{\partial t}\hat{\phi} \\ \rho\hat{C}\frac{\partial}{\partial t}T &= k_{qT}\nabla^2 T + \rho\frac{\hat{L}}{\hat{\phi}_{\max}}\hat{\sigma}_{\phi} \end{aligned}$$

View Article Online
DOI: 10.1039/D6SM00323K

$$\rho\frac{\partial}{\partial t}\hat{\phi}+\boldsymbol{\nabla\cdot\phi}-\rho\hat{\sigma}_\phi = 0$$

$$\rho\frac{\partial}{\partial t}\hat{\phi} = k_{\phi\phi}\nabla^2\hat{\phi}+\rho\hat{\sigma}_\phi$$

assuming a constant latent heat and transport properties. The last form of the energy equation follows by substitution of the equation for $\hat{\phi}$. Note also that we have switched $\sigma_\phi \to \rho\hat{\sigma}_\phi$

There are still conditions on the term $B\sigma_\phi$ that need to be satisfied. At equilibrium this term must vanish. If we expect specific values of $\hat{\phi}$ at equilibrium then these should appear as roots of this function. For example suppose one expects

$$\hat{\phi} = 0 \text{ for } T > T_m$$

$$\hat{\phi} = \hat{\phi}_{\max} \text{ for } T < T_m$$

as one might for crystallization. Then a reasonable form would be

$$\sigma_\phi(T,\hat{\phi}) = f(T)\hat{\phi}\left(\hat{\phi}_{\max}-\hat{\phi}\right)$$

Out of equilibrium one must have

$$B\sigma_\phi = -\frac{1}{T}\frac{\partial\hat{A}}{\partial\hat{\phi}}\sigma_\phi(T,\hat{\phi}) = -\frac{1}{T\hat{\phi}_{\max}}\left(\hat{A}_S(T)-\hat{A}_L(T)\right)\sigma_\phi(T,\hat{\phi}) \geq 0$$

$$\frac{\partial\hat{A}}{\partial\hat{\phi}} = \frac{\hat{A}_S}{\hat{\phi}_{\max}}(T)-\frac{\hat{A}_L}{\hat{\phi}_{\max}}(T) \equiv \frac{1}{\hat{\phi}_{\max}}\left(\hat{A}_S(T)-\hat{A}_L(T)\right)$$

For crystallization the function $\left(\hat{A}_S(T)-\hat{A}_L(T)\right)$ has the behavior

$$\left(\hat{A}_S(T)-\hat{A}_L(T)\right) > 0 \text{ for } T > T_m$$

$$\left(\hat{A}_S(T)-\hat{A}_L(T)\right) < 0 \text{ for } T < T_m$$

$$\left(\hat{A}_S(T)-\hat{A}_L(T)\right) = 0 \text{ for } T = T_m$$

Taylor expanding from T_m leads to

$$\begin{aligned}\left(\hat{A}_S(T)-\hat{A}_L(T)\right) &\simeq \hat{A}_S(T_m)+\left(\frac{\partial\hat{A}_S}{\partial T}\right)_{T_m}(T-T_m)\\ &- \hat{A}_L(T_m)-\left(\frac{\partial\hat{A}_L}{\partial T}\right)_{T_m}(T-T_m)\\ &= \left(\hat{S}_L(T_m)-\hat{S}_S(T_m)\right)(T-T_m)\\ &= \Delta\hat{S}_{melt}(T_m)(T-T_m)\\ -\frac{1}{T}\frac{\partial\hat{A}}{\partial\hat{\phi}} &= -\frac{1}{T\hat{\phi}_{\max}}\left(\hat{A}_S(T)-\hat{A}_L(T)\right)\\ &= -\frac{\Delta\hat{S}_{melt}}{\hat{\phi}_{\max}}(T_m)\left(1-\frac{T_m}{T}\right) = \frac{\Delta\hat{S}_{melt}}{\hat{\phi}_{\max}}\left(\frac{T_m}{T}-1\right)\end{aligned}$$

which conforms to the expectations indicated above. Then a reasonable simplest form consistent with the second law inequality is

$$\begin{aligned}B\sigma_\phi &= -\frac{1}{T}\frac{\partial\hat{A}}{\partial\hat{\phi}}\sigma_\phi(T,\hat{\phi}) = -\frac{1}{T\hat{\phi}_{\max}}\left(\hat{A}_S(T)-\hat{A}_L(T)\right)\sigma_\phi(T,\hat{\phi}) \geq 0\\ &= -\frac{1}{T\hat{\phi}_{\max}}\Delta\hat{S}_{melt}(T_m)(T-T_m)\ \sigma_\phi(T,\hat{\phi}) \geq 0\\ &= -\frac{T_m}{T\hat{\phi}_{\max}}\Delta\hat{S}_{melt}(T_m)\left(\frac{T}{T_m}-1\right)\ \sigma_\phi(T,\hat{\phi}) \geq 0\\ &\Rightarrow \quad \sigma_\phi(T,\hat{\phi}) \sim \left(1-\frac{T}{T_m}\right)\hat{\phi}\left(\hat{\phi}_{\max}-\hat{\phi}\right)\end{aligned}$$

Notice where $T > T_m \Rightarrow \sigma_\phi(T,\hat{\phi}) < 0$ and the source term drives the system to the liquid state ($\hat{\phi}=0$). If $T < T_m \Rightarrow \sigma_\phi(T,\hat{\phi}) > 0$ and the source term drives the system to the solid state ($\hat{\phi}=\hat{\phi}_{\max}$).

B Appendix B: Numerical Methods for 1 and 2 Dimensional Calculations

We use the Method of Lines (MOL) to convert our PDEs to a set of ODEs to further integrate using the implicit and explicit numerical schemes. Using the central difference for the second order derivative, we define,

$$\frac{\partial^2\theta}{\partial\chi^2} = \frac{\theta_{i+1}-2\theta_i+\theta_{i-1}}{\Delta\chi^2}$$

Similarly, using the central difference for the first order derivative, we define,

$$\frac{\partial\theta}{\partial\chi} = \frac{\theta_{i+1}-\theta_{i-1}}{2\Delta\chi}$$

Consider the one dimensional computational domain from $\chi = 0$ to $\chi = L$. The entire domain is discretised into a grid with a spacing of $\Delta\chi$, and hence the temperature and order parameter take discrete values θ_i and ϕ_i respectively. Here, the subscript i stands for the i-th grid point. For two-dimensional calculations, we use a grid of 300×300 points. We use $\Delta\chi = 0.25$. The Δt then is chosen based on the stability criterion $\frac{1}{2} \geq \frac{\Delta t}{(\Delta\chi)^2}$. Explicit Euler scheme is used for solving the order parameter equation and an implicit Euler for the energy equation using an in-house Python code. The simulations are independently verified using ode15s solver in MATLAB. An initial condition for θ and ϕ is specified at all grid points. As discussed in the main text, either a constant temperature $\theta = -1$ or a Neumann boundary condition $\partial\phi/\partial\chi = 0$ is imposed on the left-hand boundary, $\chi = 0$. Similar boundary conditions are used for the order parameter (ϕ) as well.

C Appendix C: Linear Stability Analysis in 1 Dimension from the Initial Quenched State

Here, we consider a one-dimensional, doubly infinite spatial domain of a subcooled melt at a temperature $T_0 < T_m$ and carry out a linear stability analysis according to the NET model.

View Article Online
DOI: 10.1039/D6SM00323K

$$\begin{aligned}
\frac{\partial}{\partial t}T &= \alpha\frac{\partial^2}{\partial x^2}T+\frac{\hat{L}}{\hat{C}}R\left(1-\frac{T}{T_m}\right)\phi\,(1-\phi)\\
\frac{\partial}{\partial t}\phi &= \alpha_{\phi\phi}\frac{\partial^2}{\partial x^2}\phi+R\left(1-\frac{T}{T_m}\right)\phi\,(1-\phi)\\
-\infty &< x<\infty\;;\;0<t<\infty\\
T(x,0) &= T_0<T_m\;;\;\phi(x,0)=0\;;\\
&\quad T \text{ and } \phi \text{ Fourier Transformable wrt } x
\end{aligned}$$

Scaling as follows

$$\begin{aligned}
\theta &= \frac{T-T_m}{T_m-T_0}=\frac{T-T_m}{\Delta T}\\
\tau &= tR\frac{\Delta T}{T_m}\;;\;\chi=\frac{x}{\sqrt{\alpha/R\frac{\Delta T}{T_m}}}
\end{aligned}$$

gives

$$\begin{aligned}
\frac{\partial}{\partial\tau}\theta &= \frac{\partial^2}{\partial\chi^2}\theta-\lambda\theta\phi\,(1-\phi)\;;\;\lambda=\frac{\hat{L}}{\hat{C}\Delta T}\\
\frac{\partial}{\partial\tau}\phi &= \beta\frac{\partial^2}{\partial\chi^2}\phi-\theta\phi\,(1-\phi)\;;\;\beta=\frac{\alpha_{\phi\phi}}{\alpha}
\end{aligned}$$

Consider the initial state as specified above and consider the weak disturbances

$$\begin{aligned}
\theta &= \theta_0+\delta\theta=-1+\delta\theta\;;\;0<\delta\theta<<1\\
\phi &= \phi_0+\delta\phi=0+\delta\phi\;;\;0<\delta\phi<<1
\end{aligned}$$

Linearize the governing equations gives

$$\begin{aligned}
\frac{\partial}{\partial\tau}\delta\theta &= \frac{\partial^2}{\partial\chi^2}\delta\theta-\lambda\,(\delta\theta-1)\,(\delta\phi)\,(1-\delta\phi)\\
&\simeq \frac{\partial^2}{\partial\chi^2}\delta\theta+\lambda\delta\phi\\
\frac{\partial}{\partial\tau}\delta\phi &= \beta\frac{\partial^2}{\partial\chi^2}\delta\phi-(\delta\theta-1)\,(\delta\phi)\,(1-\delta\phi)\\
&\simeq \beta\frac{\partial^2}{\partial\chi^2}\delta\phi+\delta\phi
\end{aligned}$$

Now presume

$$\begin{aligned}
\delta\theta(\chi,t) &= \Theta_0 e^{iq_\theta\chi}e^{\Sigma_\theta\tau}\\
\delta\phi(\chi,t) &= \Phi_0 e^{iq_\phi\chi}e^{\Sigma_\phi\tau}
\end{aligned}$$

where the Σ_i are growth exponents. Substituting into the linearized equations from the (unstable) initial state leads to

$$\begin{aligned}
\frac{\partial}{\partial\tau}\delta\theta &= \frac{\partial^2}{\partial\chi^2}\delta\theta+\lambda\delta\phi\\
\Sigma_\theta\Theta_0 e^{iq_\theta\chi}e^{\Sigma_\theta\tau} &= -q_\theta^2\Theta_0 e^{iq_\theta\chi}e^{\Sigma_\theta\tau}+\lambda\Phi_0 e^{iq_\phi\chi}e^{\Sigma_\phi\tau}\\
\Sigma_\theta &= -q_\theta^2+\lambda\frac{\Phi_0}{\Theta_0}e^{i(q_\phi-q_\theta)\chi}e^{(\Sigma_\phi-\Sigma_\theta)\tau}
\end{aligned}$$

$$\begin{aligned}
\frac{\partial}{\partial\tau}\delta\phi &= \beta\frac{\partial^2}{\partial\chi^2}\delta\phi+\delta\phi\\
\Sigma_\phi\Phi_0 e^{iq_\phi\chi}e^{\Sigma_\phi\tau} &= -\beta q_\phi^2\Phi_0 e^{iq_\phi\chi}e^{\Sigma_\phi\tau}+\Phi_0 e^{iq_\phi\chi}e^{\Sigma_\phi\tau}\\
\Sigma_\phi &= 1-\beta q_\phi^2\\
\Sigma_\phi &= 1-\beta q_\phi^2
\end{aligned}$$

Harmonic perturbations in ϕ from the initial quenched state are unstable for $q^2<\frac{1}{\beta}=\frac{\alpha}{\alpha_{\phi\phi}}$.

D Appendix D: Phase Space Analysis of Steady Traveling Waves in 1 Dimension

Here we visit a phase space analysis of the scaled NET model. The model in a moving frame

$$\eta=\chi-v\tau$$

and assuming a steady state is

$$\begin{aligned}
-v\frac{d}{d\eta}\theta &= \frac{d^2}{d\eta^2}\theta-\lambda\theta\phi(1-\phi)\\
-v\frac{d}{d\eta}\phi &= \beta\frac{d^2}{d\eta^2}\phi-\theta\phi(1-\phi)
\end{aligned}$$

where v is TBD. On physical grounds one expects $\beta<O(10^0)$ while $\lambda\geq O(10^0)$. Presumably

$$v=v(\beta,\lambda)$$

The auxiliary conditions are

$$\begin{aligned}
\lim_{\eta\to-\infty}\begin{pmatrix}\theta\\ \phi\end{pmatrix} &= \begin{pmatrix}\theta_{ss}\\ \phi_{ss}\end{pmatrix}\\
\lim_{\eta\to\infty}\begin{pmatrix}\theta\\ \phi\end{pmatrix} &= \begin{pmatrix}-1\\ 0\end{pmatrix}
\end{aligned}$$

which introduces two additional parameters, θ_{ss} and ϕ_{ss}, related by a global energy balance constraint which, can be derived from the moving frame, steady ODEs and the BCs for an adiabatic wave.

$$(1+\theta_{ss})=\lambda\phi_{ss}$$

View Article Online
DOI: 10.1039/D6SM00323K

An equivalent fourth order autonomous system is

$$\begin{aligned}\frac{d}{d\eta}\theta &= u\\ \frac{d}{d\eta}u &= \lambda\theta\phi(1-\phi)-vu\\ \frac{d}{d\eta}\phi &= \gamma\\ \frac{d}{d\eta}\gamma &= \frac{1}{\beta}\theta\phi(1-\phi)-\frac{v}{\beta}\gamma\end{aligned}$$

The critical points satisfy

$$\begin{aligned}u &= 0\\ \lambda\theta\phi(1-\phi)-vu &= 0\\ \gamma &= 0\\ \theta\phi(1-\phi)-v\gamma &= 0\end{aligned}$$

Denoting each as an ordered quartet (θ,u,ϕ,γ) the critical points are

$$(0,0,\phi_{ss},0)$$

$$(\theta_{ss},0,0,0)$$

$$(\theta_{ss},0,1,0)$$

where it is recognized that $u=\gamma=0$ corresponds to far-field left or right. If one makes use of the global constraint $(1+\theta_{ss})=\lambda\phi_{ss}$ these become

$$\left(0,0,\frac{1}{\lambda},0\right)$$

$$(-1,0,0,0)$$

$$(\lambda-1,0,1,0)$$

The nature of each follows from local stability analyses.
We use the stability analysis summarized by Roussel[36] without introducing the global constraint at first. Denoting

$$\mathbf{x}=\begin{pmatrix}\theta\\ u\\ \phi\\ \gamma\end{pmatrix}$$

and by $\mathbf{x}^*$ the values at the critical points. Further, denote

$$\mathbf{f}(\mathbf{x})=\begin{pmatrix}f_1(\theta,u,\phi,\gamma)\\ f_2(\theta,u,\phi,\gamma)\\ f_3(\theta,u,\phi,\gamma)\\ f_4(\theta,u,\phi,\gamma)\end{pmatrix}=\begin{pmatrix}u\\ \lambda\theta\phi(1-\phi)-vu\\ \gamma\\ \frac{1}{\beta}\theta\phi(1-\phi)-\frac{v}{\beta}\gamma\end{pmatrix}$$

Then linearizing

$$\frac{d}{d\eta}\mathbf{x}=\mathbf{f}(\mathbf{x})$$

via a Taylor expansion near a critical point leads to

$$\frac{d}{d\eta}\delta\mathbf{x}=\mathbf{J}(\mathbf{x}^*)\cdot\delta\mathbf{x}$$

where

$$\delta\mathbf{x}=\mathbf{x}-\mathbf{x}^*$$

and the Jacobian $\mathbf{J}(\mathbf{x})$ is

$$\mathbf{J}(\mathbf{x})=\begin{pmatrix}\frac{\partial}{\partial\theta}f_1 & \frac{\partial}{\partial u}f_1 & \frac{\partial}{\partial\phi}f_1 & \frac{\partial}{\partial\gamma}f_1\\ \frac{\partial}{\partial\theta}f_2 & \frac{\partial}{\partial u}f_2 & \frac{\partial}{\partial\phi}f_2 & \frac{\partial}{\partial\gamma}f_2\\ \frac{\partial}{\partial\theta}f_3 & \frac{\partial}{\partial u}f_3 & \frac{\partial}{\partial\phi}f_3 & \frac{\partial}{\partial\gamma}f_3\\ \frac{\partial}{\partial\theta}f_4 & \frac{\partial}{\partial u}f_4 & \frac{\partial}{\partial\phi}f_4 & \frac{\partial}{\partial\gamma}f_4\end{pmatrix}$$

$$=\begin{pmatrix}0 & 1 & 0 & 0\\ \lambda\phi(1-\phi) & -v & \lambda\theta(1-2\phi) & 0\\ 0 & 0 & 0 & 1\\ \frac{1}{\beta}\phi(1-\phi) & 0 & \frac{1}{\beta}\theta(1-2\phi) & -\frac{v}{\beta}\end{pmatrix}$$

The linear stability characteristics for each critical point can be reckoned from the eigenvalues of the Jacobian evaluated there.

At the second critical point $\mathbf{x}^*=\begin{pmatrix}\theta_{ss}\\ 0\\ 0\\ 0\end{pmatrix}$ and

$$\mathbf{J}(\mathbf{x}^*)=\begin{pmatrix}0 & 1 & 0 & 0\\ 0 & -v & \lambda\theta_{ss} & 0\\ 0 & 0 & 0 & 1\\ 0 & 0 & \frac{1}{\beta}\theta_{ss} & -\frac{v}{\beta}\end{pmatrix}$$

The eigenvalues are

$$\begin{aligned}k_1 &= -\frac{1}{2\beta}\left(v-\sqrt{v^2+4\theta_{ss}\beta}\right)\\ k_2 &= -\frac{1}{2\beta}\left(v+\sqrt{v^2+4\theta_{ss}\beta}\right)\\ k_3 &= -v<0\\ k_4 &= 0\end{aligned}$$

The condition

$$v^2+4\theta_{ss}\beta\geq 0$$

avoids unphysical oscillatory behavior (spirals). This ensures

$$k_2<0$$

Further $v-\sqrt{v^2+4\theta_{ss}\beta}>0$

$$\begin{aligned}v &> \sqrt{v^2+4\theta_{ss}\beta}\\ v^2 &> v^2+4\theta_{ss}\beta\end{aligned}$$

is guaranteed so that

$$k_2<0$$

View Article Online
DOI: 10.1039/D6SM00323K

and this critical point appears to be stable under this constraint, except for the fact that $k_4 = 0$ which indicates a central manifold whose stability characteristics could be explored further. We do not pursue this but rely on numerical results for verification of the stability at this critical point (see main text).

For the moment we note that if

$$v^2 + 4\theta_{ss}\beta = 0$$

and under the assignment $\theta_{ss} = -1$ consistent with the far field right boundary conditions ($\phi_{ss} = 0$) of this critical point one finds the selection

$$v = 2\sqrt{\beta}$$

consistent with numerical data showing $v \sim \sqrt{\beta}$. Then the eigenvalues are

$$\begin{aligned} k_1 &= -\frac{1}{\sqrt{\beta}} \\ k_2 &= -\frac{1}{\sqrt{\beta}} \\ k_3 &= -2\sqrt{\beta} \\ k_4 &= 0 \end{aligned}$$

and we get a repeated negative eigenvalue. It appears this critical point is stable, although there appears a null eigen value $k_4 = 0$.

The other two critical points indicate instability. At the first critical point $\mathbf{x}^* = \begin{pmatrix} 0 \\ 0 \\ \phi_{ss} \\ 0 \end{pmatrix}$ one has

$$\mathbf{J}(\mathbf{x}^*) = \begin{pmatrix} 0 & 1 & 0 & 0 \\ \lambda\phi_{ss}(1-\phi_{ss}) & -v & 0 & 0 \\ 0 & 0 & 0 & 1 \\ \frac{1}{\beta}\phi_{ss}(1-\phi_{ss}) & 0 & 0 & -\frac{v}{\beta} \end{pmatrix}$$

The eigenvalues are

$$\begin{aligned} k_1 &= -\frac{1}{2}v + \frac{1}{2}\sqrt{v^2 + 4\lambda\phi_{ss}(1-\phi_{ss})} > 0 \\ k_2 &= -\frac{1}{2}v - \frac{1}{2}\sqrt{v^2 + 4\lambda\phi_{ss}(1-\phi_{ss})} < 0 \\ k_3 &= -\frac{v}{\beta} < 0 \\ k_4 &= 0 \end{aligned}$$

which appears to be unstable (saddle point). Note the global constraint $(1+\theta_{ss}) = \lambda\phi_{ss}$ suggests that at this critical point, where $\theta_{ss} = 0 \Rightarrow \phi_{ss} = \frac{1}{\lambda}$. The domain of ϕ_{ss} $(0 \le \phi_{ss} \le 1)$ restricts this as a critical point to values $\lambda > 1$. The eigenvalues are than

$$\begin{aligned} k_1 &= -\frac{1}{2}v + \frac{1}{2}\sqrt{v^2 + 4\left(1-\frac{1}{\lambda}\right)} > 0\ ;\ \lambda > 1 \\ k_2 &= -\frac{1}{2}v - \frac{1}{2}\sqrt{v^2 + 4\left(1-\frac{1}{\lambda}\right)} < 0\ ;\ \lambda > 1 \\ k_3 &= -\frac{v}{\beta} < 0 \\ k_4 &= 0 \end{aligned}$$

Furthermore if we assign $v = 2\sqrt{\beta}$ these become

$$\begin{aligned} k_1 &= -\sqrt{\beta} + \sqrt{\beta + \left(1-\frac{1}{\lambda}\right)} > 0\ ;\ \lambda > 1 \\ k_2 &= -\sqrt{\beta} - \frac{1}{2}\sqrt{\beta + \left(1-\frac{1}{\lambda}\right)} < 0\ ;\ \lambda > 1 \\ k_3 &= -\frac{2}{\sqrt{\beta}} < 0 \\ k_4 &= 0 \end{aligned}$$

indicating instability. At the final critical point $\mathbf{x}^* = \begin{pmatrix} \theta_{ss}0 \\ 1 \\ 0 \end{pmatrix}$ one finds

$$\mathbf{J}(\mathbf{x}^*) = \begin{pmatrix} 0 & 1 & 0 & 0 \\ 0 & -v & -\lambda\theta_{ss} & 0 \\ 0 & 0 & 0 & 1 \\ 0 & 0 & -\frac{1}{\beta}\theta_{ss} & -\frac{v}{\beta} \end{pmatrix}$$

The eigen values are

$$\begin{aligned} k_1 &= -\frac{1}{2\beta}\left(v - \sqrt{v^2 - 4\theta_{ss}\beta}\right) > 0 \\ k_2 &= -\frac{1}{2\beta}\left(v + \sqrt{v^2 - 4\theta_{ss}\beta}\right) < 0 \\ k_3 &= -v < 0 \\ k_4 &= 0 \end{aligned}$$

indicating instability. Considering $\phi_{ss} = 1$ at this critical point, the global constraint $(1+\theta_{ss}) = \lambda\phi_{ss} \Rightarrow \theta_{ss} = \lambda - 1$. The domain of θ_{ss} $(-1 \le \theta_{ss} \le 0)$ restricts this as a critical point to values $\lambda < 1$. The eigenvalues would be

$$\begin{aligned} k_1 &= -\frac{1}{2\beta}\left(v - \sqrt{v^2 - 4(\lambda-1)\beta}\right) > 0\ ;\ \lambda < 1 \\ k_2 &= -\frac{1}{2\beta}\left(v + \sqrt{v^2 - 4(\lambda-1)\beta}\right) < 0\ ;\ \lambda < 1 \\ k_3 &= -v < 0 \\ k_4 &= 0 \end{aligned}$$

View Article Online
DOI: 10.1039/D6SM00323K

Furthermore if we assign $v = 2\sqrt{\beta}$ these become

$$\begin{aligned} k_1 &= -\frac{1}{\sqrt{\beta}}\left(1-\sqrt{2-\lambda}\right) > 0\ ;\ \lambda < 1 \\ k_2 &= -\frac{1}{\sqrt{\beta}}\left(1+\sqrt{2-\lambda}\right) < 0\ ;\ \lambda < 1 \\ k_3 &= -2\sqrt{\beta} < 0 \\ k_4 &= 0 \end{aligned}$$

indicating instability.

E Appendix E: Including Interfacial Energy in the NET Model

This section summarizes revisions to the development in Appendix A: Non Equilibrium Thermodynamics (NET) Model to include interfacial energy at the simplest level. Concerning the specific form of the free energy for (partially) solidified materials reasonable assertion is

$$\begin{aligned} \hat{A}\left(\hat{\phi},T\right) &= \hat{A}_S(T)\,\phi + \hat{A}_L(T)\,(1-\phi)\ ;\ \phi = \frac{\hat{\phi}}{\hat{\phi}_{\max}} \\ &= \hat{A}_L(T) + \left(\hat{A}_S(T) - \hat{A}_L(T)\right)\phi \end{aligned}$$

where $\hat{\phi}_{\max}$ is a maximum value of $\hat{\phi}$, and the subscripts indicate the phase (S for solid and L for liquid). Then

$$\frac{\partial \hat{A}}{\partial \hat{\phi}} = \frac{\hat{A}_S}{\hat{\phi}_{\max}}(T) - \frac{\hat{A}_L}{\hat{\phi}_{\max}}(T) \equiv \frac{1}{\hat{\phi}_{\max}}\left(\hat{A}_S(T) - \hat{A}_L(T)\right)$$

This expression ignores interfacial free energy. Interfacial free energy can be included in a simple, approximate way. Consider

$$\begin{aligned} \hat{A}\left(\hat{\phi},T\right) &= \hat{A}^{\infty}_S(T)\,\phi + \hat{A}^{\infty}_L(T)\,(1-\phi) + \hat{A}_{int}(T,\phi)\ \ ;\ \phi = \frac{\hat{\phi}}{\hat{\phi}_{\max}} \\ &= \hat{A}^{\infty}_L(T) + \left(\hat{A}^{\infty}_S(T) - \hat{A}^{\infty}_L(T)\right)\phi + \hat{A}_{int}(T,\phi) \end{aligned}$$

where the superscript ∞ indicates the bulk values, and $\hat{A}_{int}(T,\phi)$ is the (strictly positive) interfacial contribution to $\hat{A}\left(\hat{\phi},T\right)$. If the semi-crystalline morphology is scale-invariant one can presume

$$\hat{A}_{int}(T,\phi) = a_s\gamma(T)\phi\ \ [=]\ \ \frac{L^2}{M}\frac{E}{L^2}$$

where

a_s - specific interfacial area of fully crystalline material

$\gamma(T)$ - interfacial energy (tension)

Consequently

$$\frac{\partial \hat{A}}{\partial \hat{\phi}} = \frac{\hat{A}^{\infty}_S(T)}{\hat{\phi}_{\max}}(T) - \frac{\hat{A}^{\infty}_L(T)}{\hat{\phi}_{\max}}(T) + \frac{a_s\gamma(T)}{\hat{\phi}_{\max}} \equiv \frac{1}{\hat{\phi}_{\max}}\left(\hat{A}^{\infty}_S(T) - \hat{A}^{\infty}_L(T)\right) + \frac{a_s\gamma(T)}{\hat{\phi}_{\max}}$$

This revision demands reconsideration of the thermodynamic restrictions on the term $B\sigma_\phi$ in the rate of entropy production. Out of equilibrium one must have

$$\begin{aligned} B\sigma_\phi &= -\frac{1}{T}\frac{\partial \hat{A}}{\partial \hat{\phi}}\,\sigma_\phi(T,\hat{\phi}) \\ &= -\frac{1}{T\hat{\phi}_{\max}}\left[\left(\hat{A}^{\infty}_S(T) - \hat{A}^{\infty}_L(T)\right) + a_s\gamma(T)\right]\sigma_\phi(T,\hat{\phi}) \geq 0 \end{aligned}$$

where we used

$$\begin{aligned} \frac{\partial \hat{A}}{\partial \hat{\phi}} &= \frac{\hat{A}^{\infty}_S(T)}{\hat{\phi}_{\max}} - \frac{\hat{A}^{\infty}_L(T)}{\hat{\phi}_{\max}} + \frac{a_s\gamma(T)}{\hat{\phi}_{\max}} \\ &\equiv \frac{1}{\hat{\phi}_{\max}}\left(\hat{A}^{\infty}_S(T) - \hat{A}^{\infty}_L(T)\right) + \frac{a_s\gamma(T)}{\hat{\phi}_{\max}} \end{aligned}$$

For crystallization, the function $\left(\hat{A}_S(T) - \hat{A}_L(T)\right)$ has the behavior

$$\begin{aligned} \left(\hat{A}^{\infty}_S(T) - \hat{A}^{\infty}_L(T)\right) &> 0 \ \ for\ \ T > T^{\infty}_m \\ \left(\hat{A}^{\infty}_S(T) - \hat{A}^{\infty}_L(T)\right) &< 0 \ \ for\ \ T < T^{\infty}_m \\ \left(\hat{A}^{\infty}_S(T) - \hat{A}^{\infty}_L(T)\right) &= 0 \ \ for\ \ T = T^{\infty}_m \end{aligned}$$

where T^{∞}_m means the (hypothetical) melting point of bulk monolithic crystal. Taylor expanding from T^{∞}_m

$$\begin{aligned} \left(\hat{A}^{\infty}_S(T) - \hat{A}^{\infty}_L(T)\right) &\simeq \hat{A}^{\infty}_S\left(T^{\infty}_m\right) + \left(\frac{\partial \hat{A}^{\infty}_S}{\partial T}\right)_{T^{\infty}_m}(T - T^{\infty}_m) - \hat{A}^{\infty}_L(T^{\infty}_m) \\ &\quad - \left(\frac{\partial \hat{A}^{\infty}_L}{\partial T}\right)_{T^{\infty}_m}(T - T^{\infty}_m) \\ &= \left(\hat{S}^{\infty}_L(T^{\infty}_m) - \hat{S}^{\infty}_S(T^{\infty}_m)\right)(T - T^{\infty}_m) \\ &= \Delta\hat{S}^{\infty}_{melt}(T^{\infty}_m)(T - T^{\infty}_m) \\ a_s\gamma(T) &\simeq a_s\gamma(T^{\infty}_m) + a_s\left(\frac{d\gamma}{dT}\right)_{T^{\infty}_m}(T - T^{\infty}_m) \end{aligned}$$

so that

$$\begin{aligned} -\frac{1}{T}\frac{\partial \hat{A}}{\partial \hat{\phi}} &= -\frac{1}{T\hat{\phi}_{\max}}\left(\hat{A}^{\infty}_S(T) - \hat{A}^{\infty}_L(T) + a_s\gamma(T)\right) \\ &= -\frac{1}{T\hat{\phi}_{\max}}\left[a_s\gamma(T^{\infty}_m)\right] \\ &\quad - \frac{1}{T\hat{\phi}_{\max}}\left[\left(\Delta\hat{S}^{\infty}_{melt}(T^{\infty}_m) + a_s\left(\frac{d\gamma}{dT}\right)_{T^{\infty}_m}\right)(T - T^{\infty}_m)\right] \\ &= -\frac{a_s\gamma(T^{\infty}_m)}{T\hat{\phi}_{\max}} \\ &\quad - \frac{1}{T\hat{\phi}_{\max}}\left(\Delta\hat{S}^{\infty}_{melt}(T^{\infty}_m) + a_s\left(\frac{d\gamma}{dT}\right)_{T^{\infty}_m}\right)(T - T^{\infty}_m) \end{aligned}$$

Then a reasonable simplest form consistent with the second law

View Article Online
DOI: 10.1039/D6SM00323K

inequality is

$$
\begin{aligned}
B\sigma_\phi &= -\frac{1}{T}\frac{\partial \hat{A}}{\partial \hat{\phi}}\,\sigma_\phi(T,\hat{\phi}) \\
&= -\frac{1}{T\hat{\phi}_{\max}}\left(\hat{A}_S^{\infty}(T)-\hat{A}_L^{\infty}(T)+a_s\gamma(T)\right)\sigma_\phi(T,\hat{\phi}) \geq 0 \\
&= \left[-\frac{a_s\gamma(T_m^{\infty})}{T\hat{\phi}_{\max}} - \frac{1}{T\hat{\phi}_{\max}}\left(\Delta\hat{S}^{\infty}_{melt}(T_m^{\infty})+a_s\left(\tfrac{d\gamma}{dT}\right)_{T_m^{\infty}}\right)(T-T_m^{\infty})\right] \\
&\times \sigma_\phi(T,\hat{\phi}) \geq 0 \\
&= -\frac{1}{T\hat{\phi}_{\max}}\left[a_s\gamma(T_m^{\infty})+\Delta\hat{S}^{eff}_{melt}(T_m^{\infty})(T-T_m^{\infty})\right]\sigma_\phi(T,\hat{\phi}) \geq 0,
\end{aligned}
$$

where $\Delta\hat{S}^{eff}_{melt}(T_m^{\infty}) = \Delta\hat{S}^{\infty}_{melt}(T_m^{\infty}) + a_s\left(\frac{d\gamma}{dT}\right)_{T_m^{\infty}} \gtrless 0.$

$$
\begin{aligned}
&= -\frac{T_m^{\infty}\Delta\hat{S}^{\infty}_{melt}(T_m^{\infty})}{T\hat{\phi}_{\max}}\left[\frac{a_s\gamma(T_m^{\infty})}{T_m^{\infty}\Delta\hat{S}^{\infty}_{melt}(T_m^{\infty})}+\frac{\Delta\hat{S}^{eff}_{melt}(T_m^{\infty})}{\Delta\hat{S}^{\infty}_{melt}(T_m^{\infty})}\frac{(T-T_m^{\infty})}{T_m^{\infty}}\right] \\
&\times \sigma_\phi(T,\hat{\phi}) \geq 0 \\
&\Rightarrow \sigma_\phi(T,\hat{\phi}) \sim -\left(\Gamma_s+\Lambda\frac{(T-T_m^{\infty})}{T_m^{\infty}}\right)\hat{\phi}(\hat{\phi}_{\max}-\hat{\phi}),
\end{aligned}
$$

where $\Gamma_s \equiv \frac{a_s\gamma(T_m^{\infty})}{T_m^{\infty}\Delta\hat{S}^{\infty}_{melt}(T_m^{\infty})} > 0, \quad \Lambda = \frac{\Delta\hat{S}^{eff}_{melt}(T_m^{\infty})}{\Delta\hat{S}^{\infty}_{melt}(T_m^{\infty})} \gtrless 0.$

Notice first, if one neglects Γ_s then when $T > T_m^{\infty} \Rightarrow \sigma_\phi(T,\hat{\phi}) < 0$ and the source term drives the system to the liquid state ($\hat{\phi} = 0$). while if $T < T_m^{\infty} \Rightarrow \sigma_\phi(T,\hat{\phi}) > 0$ and the source term drives the system to the solid state ($\hat{\phi} = \hat{\phi}_{\max}$). Including the (strictly positive, presumably small) constant Γ_s effectively suppresses the melting point to T_m

$$
\begin{aligned}
\Gamma_s+\Lambda\frac{(T_m-T_m^{\infty})}{T_m^{\infty}} &= 0 \\
\Rightarrow \quad T_m &= T_m^{\infty}\left(1-\frac{\Gamma_s}{\Lambda}\right)
\end{aligned}
$$

This is a form of the Gibbs-Thomson relation.

Author contributions

Sameer Rajendra Kalghatgi: conceptualization, data curation, formal analysis, investigation, methodology, validation, software, project administration, visualization, writing (original draft, review and editing); Sumesh P. Thampi: conceptualization, project administration, supervision, writing (review and editing); Sanat K. Kumar: conceptualization, project administration, supervision, writing (review and editing); Christopher J. Durning: conceptualization, formal analysis, investigation, methodology, project administration, visualization, writing (original draft, review and editing)

Conflicts of interest

There are no conflicts of interest to declare.

Data availability

Python and MATLAB codes were used for the simulations and analyses, and are available upon request.

Acknowledgements

S.K.K acknowledges the financial support from the U.S. Department of Energy, Office of Science, Office of Basic Energy Sciences, Division of Material Sciences and Engineering under Award DE-SC0018111. S.P.T acknowledges financial support from Ministry of Education Scheme for Transformational and Advanced Research in Sciences under grant MoE-STARS/STARS-2/2023-0019.

Notes and references

1 B. Lotz, T. Miyoshi and S. Z. D. Cheng, *Macromolecules*, 2017, **50**, 5995–6025.
2 N. F. Mendez, M. Martell, M. Król, V. Pai, I. C. Huang, J. Ruokolainen, F. Sansoz, A. J. Müller, L. Schadler and S. K. Kumar, *Macromolecules*, 2025, **58**, 1289–1297.
3 T. P. H. Lodge, *Polymer chemistry*, CRC Press, London, England, 2020.
4 J. M. Schultz, *Macromolecules*, 2012, **45**, 6299–6323.
5 J. S. Langer, *Rev. Mod. Phys.*, 1980, **52**, 1–28.
6 J. D. Hoffman, G. T. Davis and J. I. Lauritzen, in *The Rate of Crystallization of Linear Polymers with Chain Folding*, ed. N. B. Hannay, Springer US, Boston, MA, 1976, pp. 497–614.
7 D. M. Sadler, *Nature*, 1987, **326**, 174–177.
8 G. Strobl, *The European Physical Journal E*, 2000, **3**, 165–183.
9 A. Kundagrami and M. Muthukumar, *The Journal of Chemical Physics*, 2007, **126**, 144901.
10 S. Zhang, Z. Wang, B. Guo and J. Xu, *POLYMER CRYSTALLIZATION*, 2021, **4**, e10173.
11 M. Muthukumar, in *Modeling Polymer Crystallization*, ed. G. Allegra, Springer Berlin Heidelberg, Berlin, Heidelberg, 2005, pp. 241–274.
12 T. Yamamoto, *Polymer*, 2004, **45**, 1357–1364.
13 *Perspectives in fluid dynamics*, ed. G. K. Batchelor, H. K. Moffatt and M. G. Worster, Cambridge University Press, Cambridge, England, 2002.
14 S. Adhikari, A. Purushothaman, A. A. Krauskopf, C. Durning, S. K. Kumar and S. P. Thampi, *Soft Matter*, 2021, **17**, 2518–2529.
15 C. J. Durning, A. Purushothaman, S. Adhikari, S. K. Kumar and S. Thampi, *ACS Macro Lett*, 2022, **11**, 1102–1106.
16 S. Adhikari, A. A. Krauskopf, S. K. Kumar, S. P. Thampi and C. J. Durning, *Soft Matter*, 2021, **17**, 7755–7768.
17 A. Purushothaman, S. Adhikari, C. Durning, S. K. Kumar and S. P. Thampi, *Soft Matter*, 2023, **19**, 4011–4020.
18 A. J. Lovinger and C. C. Gryte, *Macromolecules*, 1976, **9**, 247–253.

View Article Online
DOI: 10.1039/D6SM00323K

19 J.-L. Barrat and J.-P. Hansen, *Basic Concepts for Simple and Complex Liquids*, Cambridge University Press, Cambridge, 2003, pp. ix–xii.
20 R. Kobayashi, *Physica D: Nonlinear Phenomena*, 1993, **63**, 410–423.
21 P. C. Hohenberg and B. I. Halperin, *Rev. Mod. Phys.*, 1977, **49**, 435–479.
22 W. J. Boettinger, J. A. Warren, C. Beckermann and A. Karma, *Annual Review of Materials Research*, 2002, **32**, 163–194.
23 K. Yin, K. Ji, L. S. Littles, R. Trivedi, A. Karma and U. G. Wegst, *Proceedings of the National Academy of Sciences*, 2023, **120**, e2210242120.
24 D. C. Venerus and H. C. OEttinger, *A Modern Course in Transport Phenomena*, Cambridge University Press, Cambridge, England, 2018.
25 B. Carnahan and etc., *Applied numerical methods*, John Wiley & Sons, Nashville, TN, 1969.
26 W. Paul, G. D. Smith, D. Y. Yoon, B. Farago, S. Rathgeber, A. Zirkel, L. Willner and D. Richter, *Phys. Rev. Lett.*, 1998, **80**, 2346–2349.
27 R. A. FISHER, *Annals of Eugenics*, 1937, **7**, 355–369.
28 A. N. Kolmogorov and N. S. Piskunov, *I.G. Petrowsky Selected Works*, CRC Press, 2019, pp. 106–132.
29 J. Canosa, *IBM Journal of Research and Development*, 1973, **17**, 307–313.
30 A. A. Krauskopf, A. M. Jimenez, E. A. Lewis, B. D. Vogt, A. J. Müller and S. K. Kumar, *ACS Macro Letters*, 2020, **9**, 1007–1012.
31 C. I. Poser and I. C. Sanchez, *Journal of Colloid and Interface Science*, 1979, **69**, 539–548.
32 Z. Wang, M. Schaller, A. Petzold, K. Saalwächter and T. Thurn-Albrecht, *Proceedings of the National Academy of Sciences*, 2023, **120**, e2217363120.
33 A. Fernández-Tena, R. A. Pérez-Camargo, O. Coulembier, L. Sangroniz, N. Aranburu, G. Guerrica-Echevarria, G. Liu, D. Wang, D. Cavallo and A. J. Müller, *Macromolecules*, 2023, **56**, 4602–4620.
34 J. Maclaine and C. Booth, *Polymer*, 1975, **16**, 191–195.
35 I. Müller, *Thermodynamics*, Pitman, 1985.
36 M. R. Roussel, *Nonlinear dynamics*, Morgan & Claypool, San Rafael, CA, 2019.

View Article Online
DOI: 10.1039/D6SM00323K

Data availability

Python and MATLAB codes were used for the simulations and analyses, and are available upon request.